Engineering patient-derived organotypic bone models for skeletal disease and osteoanabolic therapy testing

Anke de Leeuw[1*], Chris Steffi[1*], Gian Nutal Schädli[1*], Amit Singh[1], Pei Jin Lim[2], Marianne Rohrbach[2], Cecilia Giunta[2], Matthias Rüger[3] and Ralph Müller[1]

[1]Institute for Biomechanics, ETH Zurich, Gloriastrasse 37/39, 8092 Zurich, Switzerland
[2]Connective Tissue Unit, Division of Metabolism and Children's Research Center, University Children's Hospital Zurich, Zurich, Switzerland
[3]Department of Pediatric Orthopaedics and Traumatology, University Children's Hospital Zurich, Zurich, Switzerland
[*]Authors contributed to this equally

Keywords: personalized medicine, organotypic bone models, 3D bioprinting, Dickkopf-1, osteogenesis imperfecta, time-lapsed micro-CT, osteoanabolic, transcriptomics, mechanical stimulation

Author contributions:
Conceptualization: ADL, CS, GNS, PJL, MRo, CG, MRu, RM
Methodology: ADL, CS, GNS, AS, PJL
Investigation: ADL, CS, GNS, AS
Visualization: ADL, GNS, AS
Supervision: MR, RM
Writing – original draft: ADL, GNS, CS, AS
Writing – review & editing: ADL, GNS, CS, AS, PJL, CG, MR, RM

Abstract

Patient-derived organotypic bone models offer insights into the pathomechanisms of genetic skeletal disorders and can act as platforms to study the osteoanabolic effect of drug therapies toward precision medicine. Here, we present a mechanically stimulated 3D bioprinted organotypic bone model developed *via* a two-step 3D bioprinting and cell seeding process of autologous cells from clinical bone samples, replicating both osteoblastic and osteocyte-like phenotypes. Osteoblasts were isolated from patient bone, encapsulated within a bioink for extrusion 3D bioprinting, and subjected to mechanical loading for 4 weeks until mineralized. These mineralized cell-laden constructs were top-seeded with fresh osteoblasts and cultured for an additional 4 weeks. Using osteogenesis imperfecta (OI) patient-derived osteoblasts and osteoblasts from a metabolically healthy patient undergoing femur osteotomy (FO), we investigated the effects of Dickkopf-1 antibody (DKK1Ab), a Wnt pathway modulator, on gene expression, collagen dynamics, mineralization, and mechanical properties. Time-lapsed micro-computed tomography revealed hypermineralization, increased fragility and structural deformities in OI constructs, while transcriptomics, collagen quantification, and immunohistochemistry demonstrated the model's ability to capture differential patient-specific responses to treatment. This model offers a powerful platform for predicting disease progression and treatment outcomes in skeletal disorders, with the potential to transform orthopaedic care from reactive fracture management to proactive, personalized intervention strategies.

1 Introduction

Patient-derived *in vitro* models offer unprecedented opportunities to predict disease progression, screen novel therapeutics and test treatment efficacy on a personalized level. This approach has now received regulatory support through the FDA's initiative to replace animal testing in drug development, particularly for monoclonal antibodies, with more effective, human-relevant methods.[1] For rare genetic skeletal disorders like osteogenesis imperfecta (OI), characterized by exceptional phenotypic heterogeneity, such patient-specific models can capture individual genetic and phenotypic variations that are often lost in animal models.[2] Patient-specific models could transform clinical decision making by enabling data-driven treatment plans that combine rehabilitation, pharmacological interventions, and surgical approaches to maximize mobility and autonomy while minimizing complications.

OI is a rare genetic disorder resulting in bone fragility[3] with over 20 genetically distinct

subtypes presenting with mild to lethal forms caused by gene mutations affecting osteoblast function, collagen structure, post-translational modification, or bone mineralization.[4] While murine models have advanced our understanding of OI pathophysiology,[5] they frequently fail to recapitulate the bone phenotypes observed in human patients, particularly in subtypes like *FKBP10*-related OI.[6–8] Moreover, treatments have shown inconsistent effects across different OI models[9] and clinical trials[10] remain challenging due to limited patient numbers, high phenotypic variability, and diverse treatment histories.[9,11] These limitations underscore the need for human-relevant *in vitro* bone models that can recapitulate patient-specific phenotypes for drug development and personalized treatment.

Despite its critical importance for bone homeostasis and remodeling, mechanical stimulation remains notably absent from current in vitro models of OI. Cyclic mechanical loading drives osteoblast-to-osteocyte differentiation,[12,13] regulates mineralization patterns, and shapes bone microarchitecture[14]—all crucial factors in OI pathophysiology. Previous *in-vitro* models have neglected this essential component,[15–18] limiting their physiological relevance and predictive capacity for therapeutic screening of bone-related drugs that have a differential response under cyclic mechanical loading.[19]

Currently, no FDA-approved treatments exist specifically for OI. Symptoms are managed with bisphosphonates, physical therapy, and surgical intervention. Recently, targeted anabolic protein therapies, such as sclerostin and Dickkopf-1 (DKK1) antibodies, have emerged as promising candidates to enhance bone formation through Wnt signaling modulation.[20–22] Preclinical studies have demonstrated DKK1 antibody therapy to increase bone mass, mineral density, and improves bone structure in rodent models.[23,24] Notably, children with OI exhibit significantly elevated serum DKK1 levels, both in untreated patients and those receiving bisphosphonate therapy.[25–27] When healthy mesenchymal stem cells were cultured with serum from OI patients, osteoblast differentiation was inhibited; however, the addition of DKK1 antibodies reversed this effect, increasing RUNX2 and collagen I mRNA expression.[25,27] Despite the potential of DKK1 antibodies to strengthen bone and reduce fractures, their effects on patient-derived OI cells remain unexplored in *in vitro* models.

In this study, we developed a biomimetic organotypic bone model with a novel two-step process comprising 3D bioprinting technology and cell seeding to recapitulate both osteoblastic and osteocyte-like phenotypes. By first maturing 3D bioprinted cell-laden scaffolds using patient-derived osteoblasts under cyclic mechanical loading,[12,13] and then coculturing with freshly seeded, autologous osteoblasts introduced to mineralizing surfaces, our model recapitulates aspects of woven bone and mineralized surface bone formation *in vitro*. Using patient-derived

osteoblasts from *FKBP10*-related OI, and metabolically healthy controls from a patient undergoing femur osteotomy, we created mechanically stimulated patient-specific organotypic bone constructs to evaluate the effects of DKK1 antibody treatment. We assessed treatment outcomes through time-lapsed microcomputed tomography (micro-CT) scans to monitor mineralization, endpoint immunohistochemical and histological characterization of extracellular matrices, mechanical testing, and transcriptomic analyses.

2 Results

2.1 Biofabrication and mechanical loading of patient-derived 3D bone models for treatment evaluation

In this study, a mechanically stimulated 3D bioprinted organotypic bone model was developed to replicate bone tissue architecture and assess patient-specific responses to osteoanabolic treatment. Primary osteoblasts isolated from bone explants from a metabolically healthy patient undergoing femoral osteotomy (FO) and a patient with *FKBP10*-related OI (OI) were expanded and encapsulated in an osteogenic bioink for extrusion-based 3D bioprinting (Fig. 1A). To promote mineralization and osteogenic differentiation, bioprinted constructs were subjected to a 4-week mechanically loaded preculture period with uniaxial cyclic compressive loading. At the end of preculture, mineralized constructs were reseeded with fresh primary osteoblasts from the same patient, allowing newly introduced cells to interact with mineralized surfaces, mimicking osteoblast-osteocyte communication *in vivo*. Following reseeding, constructs were cultured for an additional 4 weeks under adaptive mechanical loading, in the presence of either 1 µg/mL Dickkopf-1 antibody (DKK1Ab), an inhibitor of the Wnt signaling antagonist DKK1, or 1 µg/mL goat IgG isotype control (IgG) to account for non-specific antigen interactions (Fig. 1B).

The organotypic bone model was designed to replicate native bone modelling, with bioprinted cell-laden filaments undergoing mineralization and subsequently recruiting fresh osteoblasts to mineralized surfaces upon reseeding. These newly introduced osteoblasts spanned the macroscale scaffold pores or lined the mineralized struts, contributing to extracellular matrix deposition and tissue maturation (Fig. 1C). To evaluate the impact of combined mechanical loading and DKK1Ab treatment on osteogenesis, a multimodal analysis workflow was applied, integrating time-lapsed micro-computed tomography (micro-CT), mechanical testing, histological assessments, confocal imaging, transcriptomic profiling, and protein quantification (Fig. 1D).

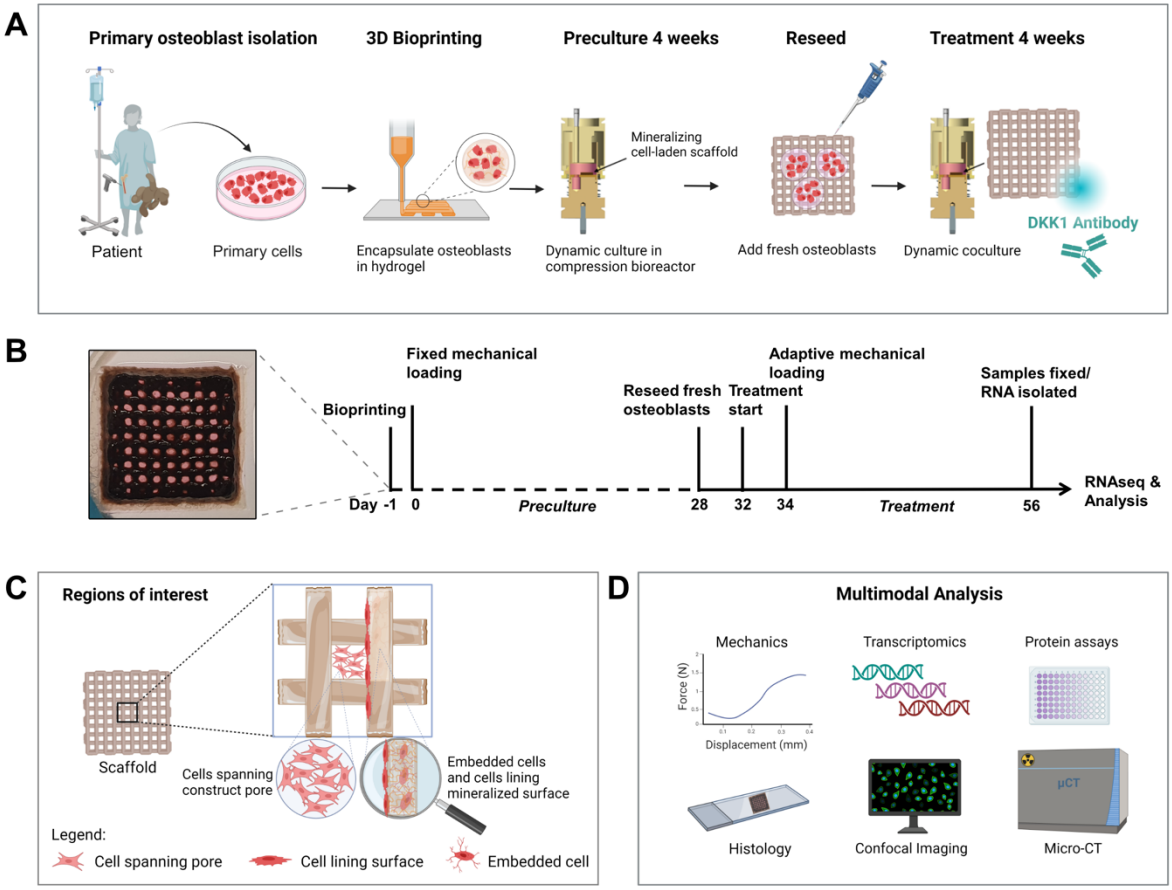

Fig. 1. Organotypic bone model study design. (A) Primary osteoblasts from metabolically healthy and *FKBP10*-OI patients' bone explants were isolated, expanded and encapsulated in osteogenic bioinks for extrusion 3D bioprinting. Cell-laden constructs were matured during 4-week preculture under uniaxial cyclic compressive loading and reseeded by pipetting fresh primary osteoblasts from the same patient on mineralized surfaces. Samples were then cultured in the presence of 1 µg/mL Dickkopf-1 antibody (DKK1Ab) or 1 µg/mL goat immunoglobulin G (IgG) isotype control under compressive loading for a further 4 weeks. (B) Experimental timeline showing bioprinted organotypic bone model, start of 4-week mechanically loaded preculture period with fixed loading (0.07N contact position preload, and cyclic compressive loading 1 % strain 5 Hz 300 sec) followed by reseeding fresh osteoblasts, start of treatment and adaptive mechanical loading (0.05N contact position + 10 % strain preload, and cyclic compressive loading 1 % strain 5 Hz 300 sec) to avoid overloading the scaffolds. (C) Schematic showing regions of interest in 3D bioprinted organotypic bone models, including mineralized surfaces of bioprinted struts and macroscale scaffold pore regions. (D) Multimodal analysis of organotypic bone models including mechanics, histology, transcriptomics, confocal imaging, protein assays and time-lapsed micro-CT scans.

2.2 OI organotypic bone models exhibit increased mineralization and loss of construct fidelity

Investigating mineralization dynamics in patients through repeated CT scans is not clinically feasible due to radiation exposure and logistical constraints. Organotypic bone models offer a patient-specific alternative, allowing longitudinal monitoring of mineralization through weekly time-lapsed micro-CT imaging (Fig. 2, Supplementary Videos 1-4). 3D reconstructions revealed fractures and a loss of fidelity in OI organotypic bone models (Fig. 2A). Loss of

fidelity and deformations in the bioprinted lattice structure became apparent after day 35 in OI samples. Visually, treatment with Dickkopf-1 antibody did not appear to reduce the fractures in the scaffold struts but did appear to reduce the severity of deformations in OI organotypic bone models (Supplementary Videos 3-4). Small mineralized structures appeared in the macroscale pores of organotypic bone models after day 35, particularly evident in the intact pores of FO samples (Supplementary Videos 5-6). In OI constructs, early mineral formation (day 7-14) was accelerated compared to FO samples (Fig. 2C), evidenced by increased mineral volume at day 21 and 28 (Fig. 2B). However, between day 28-35 mineral formation in OI dropped significantly, coinciding with loss of fidelity, leading to a plateau in mineral volume in both treated and control groups. Mineral density was significantly higher in OI groups compared to FO groups throughout the duration of the study (Fig. 2D).

To assess the mechanical properties of organotypic bone models, we performed uniaxial compressive tests and found that stiffness did not change significantly between groups (Fig. 2E). Plotting sample mineral density against stiffness (Fig. 2F), FO + IgG samples show a correlation similar to previous studies,[13] where an increase in mineral density is accompanied by in an increase in stiffness. In contrast, in the FO + DKK1Ab group, one sample with very high stiffness presented a mineral density that was lower than expected. Whereas, in OI samples, a clear correlation between mineral density and stiffness in treated or untreated samples could not be found. Global micro-CT analysis revealed differences in mineralization between organotypic bone models from each patient, including altered mineral formation rates, mineral volumes, and increased mineral density.

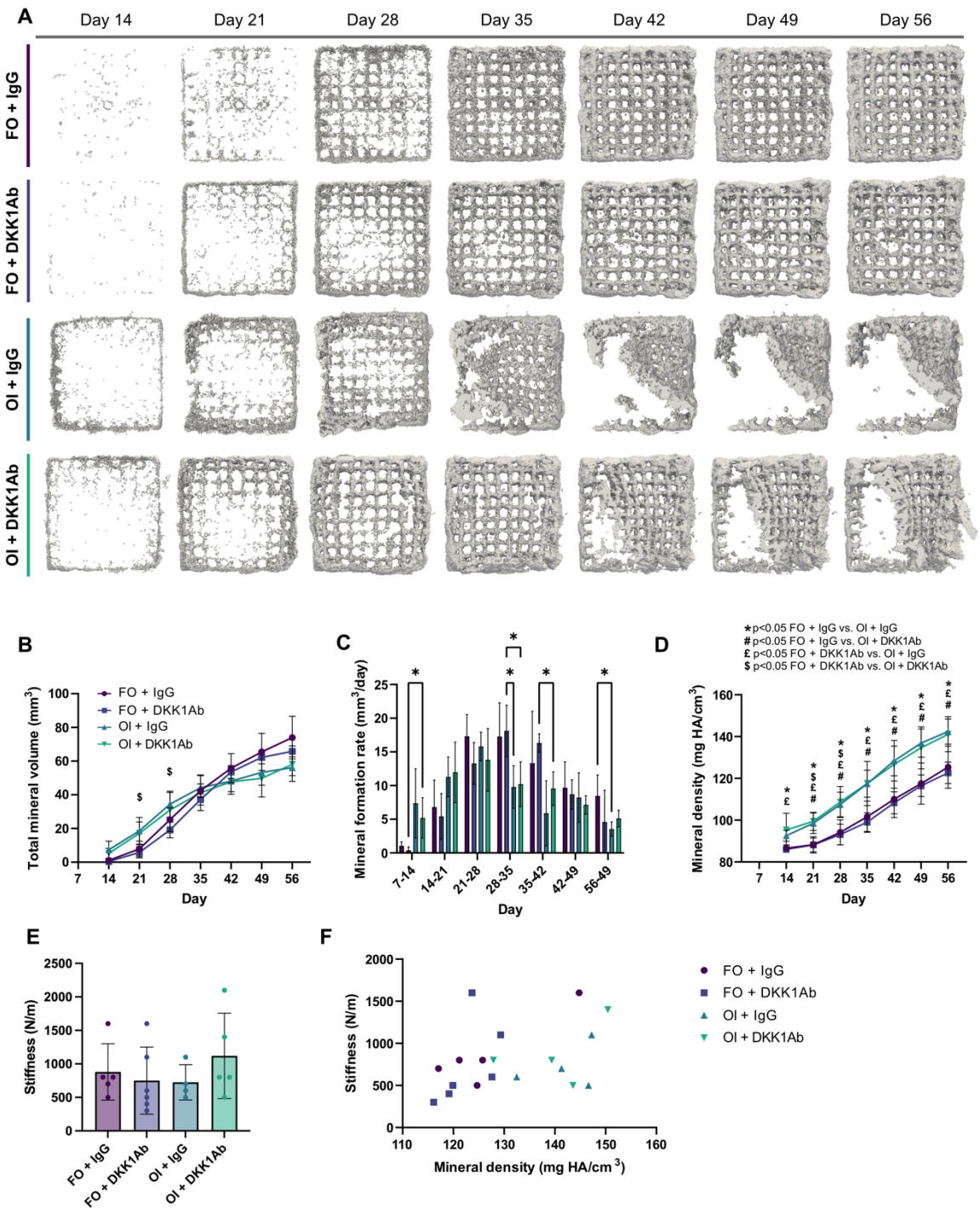

Fig. 2. Longitudinal monitoring of mineralization and endpoint stiffness of organotypic bone models. (A) Time-lapsed 3D reconstructions of representative organotypic bone models. (B) Total mineral volume, (C) Mineral formation rate (mineral volume changes over time) and, (D) Mineral density. Data are shown as mean ± standard deviation ($n \geq 5$). Statistical analysis was performed using two-way ANOVA followed by Tukey's multiple comparisons test. Symbols indicate statistical significance $p<0.05$; * was used to compare mineral density between patients i.e. FO + IgG with OI + IgG; # was used to compare FO + IgG with OI + DKK1Ab; £ was used to compare FO + DKK1Ab versus OI + IgG; $ was used to compare FO + DKK1Ab versus OI + DKK1Ab. (E) Endpoint stiffness revealed no significant differences between groups (F) Correlation of stiffness to mineral density at day 56. FO samples show correlations similar to previous work,[13] positive relationship between mineral density and resulting stiffness. OI sample mineral density is not well correlated to stiffness.

2.3 DKK1Ab treatment alters surface mineralization in organotypic bone models

To further explore whether reseeded cells increase extracellular matrix deposition and mineralization on construct surfaces, we applied an image processing method to time-lapsed micro-CT images to distinguish between bulk and surface mineralization. The administration of anti-DKK1 was initiated four weeks into the experiment, at which point the bulk of the 3D bioprinted constructs had already undergone significant mineralization, potentially masking treatment effects in global micro-CT analyses. Investigating the influence of DKK1 inhibition on reseeded cells required separating mineralization effects on the construct surface from those within the bulk structure. Therefore, we analysed registered micro-CT images spanning days 28-56 following anti-DKK1 treatment initiation to characterize structural integrity and surface-specific changes in our organotypic bone models (Fig. 3). The analysis focused on distinguishing engineered tissue volume deformation, stability, and loss across FO, OI and corresponding treatment groups and quantifying reduction in pore space due to surface mineralization.

Fig. 3A displays the structural progression of engineered tissue volume, categorizing volumes as Deformed (orange), Stable (grey), or Lost (purple) relative to the day 28 baseline. FO organotypic bone models maintained remarkable structural integrity throughout the experiment, with both treatment conditions exhibiting minimal volume loss. In contrast, OI organotypic bone models demonstrated profound structural deterioration.

The visual representation of pore spaces reveals progressive reduction in pore space in FO constructs, while OI constructs showed more erratic patterns with areas of both increased and reduced pore space (Fig. 3B), corresponding to volume loss and deformations observed in Fig. 3A. Quantitative analysis of Lost Volume (Fig. 3C) confirmed significant differences between FO and OI organotypic bone models ($p < 0.001$). FO constructs maintained stability with less than 5% volume loss in both treatment conditions (4.23% for FO + DKK1Ab and 4.34% for FO + IgG by day 56), attributable primarily to compaction from regular cyclic loading. OI constructs, in contrast, exhibited progressive volume loss, reaching 26.17% in OI + IgG constructs compared to 9.67% in OI + DKK1Ab constructs by day 56 ($p < 0.01$), indicating that DKK1 inhibition provided protection against structural deformation in the OI disease model. In constructs maintaining structural integrity (Lost Volume < 5%), we analysed Pore Space changes as an indicator of surface mineralization (Fig. 3D). The Pore Space reduced from 100% at day 28 to 74.71% in FO + IgG and 68.51% in FO + DKK1Ab by day 56, reflecting continued surface mineralization. FO + DKK1Ab constructs showed significantly reduced pore space compared to FO + IgG controls, specifically at day 49 (69.96% vs. 77.72%, $p = 0.035$). The

mixed effects model revealed significant main effects of both treatment group ($p < 0.001$) and timepoint ($p < 0.001$) on pore space dynamics, though the overall group-by-timepoint interaction did not reach statistical significance across all timepoints, indicating that the beneficial effect of DKK1 on mineralization is time-dependent and potentially transient.

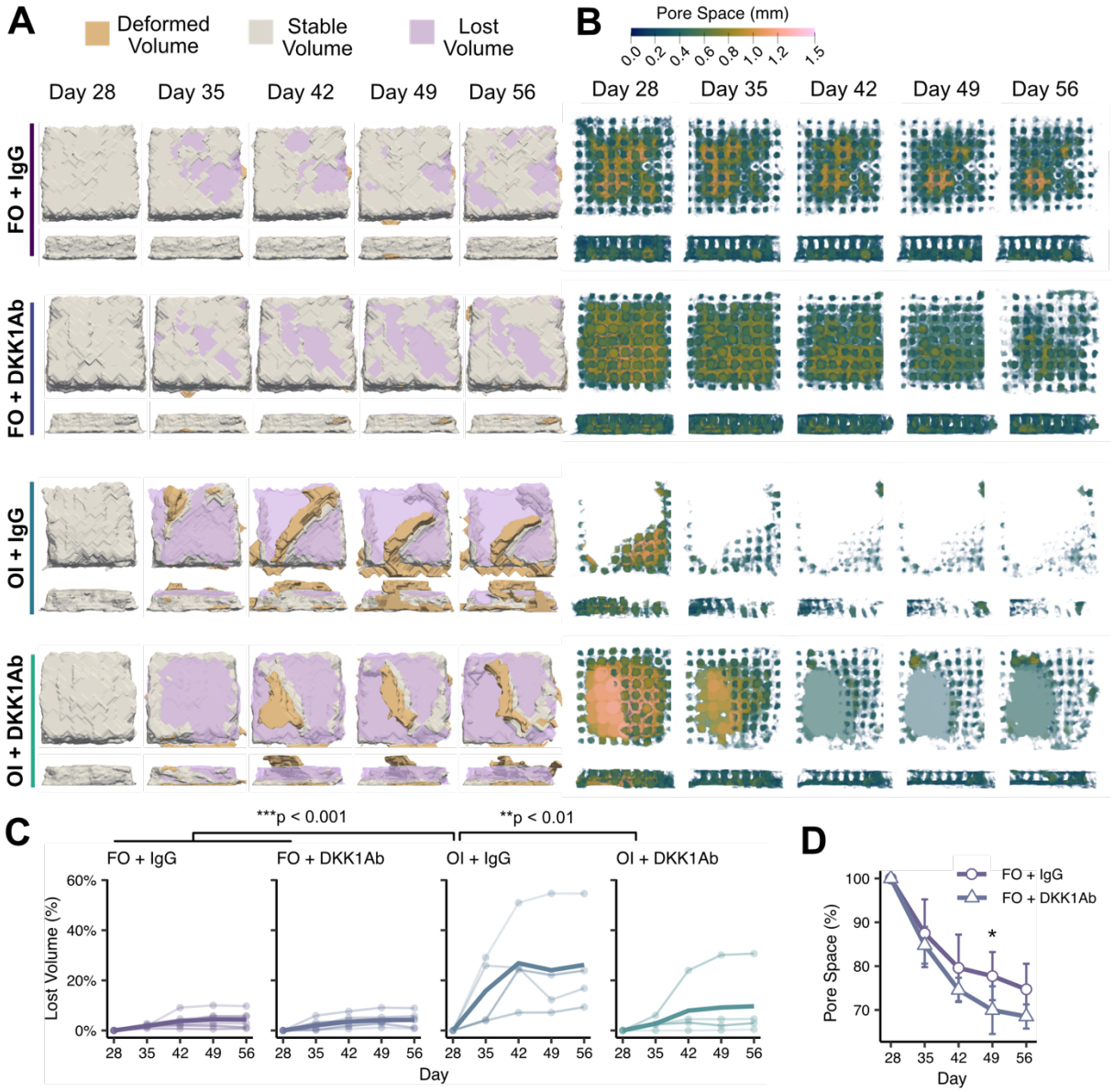

Fig. 3. Fracture and surface mineralization analysis in organotypic bone models. (A) Registered time-lapsed micro-CT images from day 28-56 for the four experimental conditions showing Deformed Volume (orange), Stable Volume (grey) and Lost Volume (purple) with day 28 as a reference time point. (B) Pore Space visualization within the region that is stable across all time points. (C) Normalized Lost Volume analysis for the four experimental conditions: for FO + DKK1Ab and FO + IgG n = 6 samples, for OI + IgG and OI + DKK1Ab n = 4 samples. (D) Normalized Pore Space analysis was performed only on experimental groups with less than 10% Lost Volume. FO + DKK1Ab was significantly different from FO + IgG on day 49 ($p = 0.035$). Statistically significant differences were tested with mixed linear models, and Bonferroni-adjusted p-values were used for post-hoc group comparisons.

2.4 Biomimetic co-culture mimics phenotypes of woven bone and surface formation in organotypic bone models

To capture phenotypic differences in ECM in patient-derived organotypic bone models, we performed histology and immunohistochemical staining. FO and OI organotypic bone models were cultured under cyclic compressive loading for 8 weeks, with a reseeding step in the middle of the culture to provide fresh osteoblasts to mineralized surfaces and macroscale pores of cell-laden scaffolds. Histological analysis showed that osteoblasts lined mineralized surfaces and produced a dense collagenous extracellular matrix (ECM) (Fig. 4A-L). H&E staining showed that cells on mineralized surfaces adopted flattened morphologies (Fig. 4A, C) while cells spanning construct pores acquired a more fibroblastic morphology (Fig. 4B, D). This differential cell localization and morphology were accompanied by a different pattern of ECM secretion. Picrosirius red staining for investigating collagen deposition revealed dense cell-secreted collagenous matrices, with cells on mineralized surfaces producing a surface-driven ECM deposited in a layered manner (Fig. 4E, G), while cells spanning macroscale construct pores produced ECM similar to woven bone filling construct pores (Fig. 4F, H). OI organotypic bone models (Fig. 2H) produced more collagen in pore regions compared to FO constructs (Fig. 4F).

The mineralized surfaces of both FO and OI samples appeared similar. Alizarin red S staining for calcium deposition showed homogenous staining in the ECM of FO construct pores (Fig. 4J) compared to the distinct mineral nodules in pores of OI samples (Fig. 4L, indicated by arrows). Collagen type I antibody staining of similar regions of interest showed higher signal in OI samples (Fig. 4O, P) compared to FO constructs (Fig. 4M, N). Similar trends in ECM organization and cell morphology were observed in DKK1Ab-treated organotypic bone models as demonstrated in supplementary histology (Fig. S2). Overall, these results indicate that this biomimetic co-culture method supports the formation of mineralized organotypic bone models mimicking features of woven bone and surface formation and reveals differences in OI and FO patient-derived models.

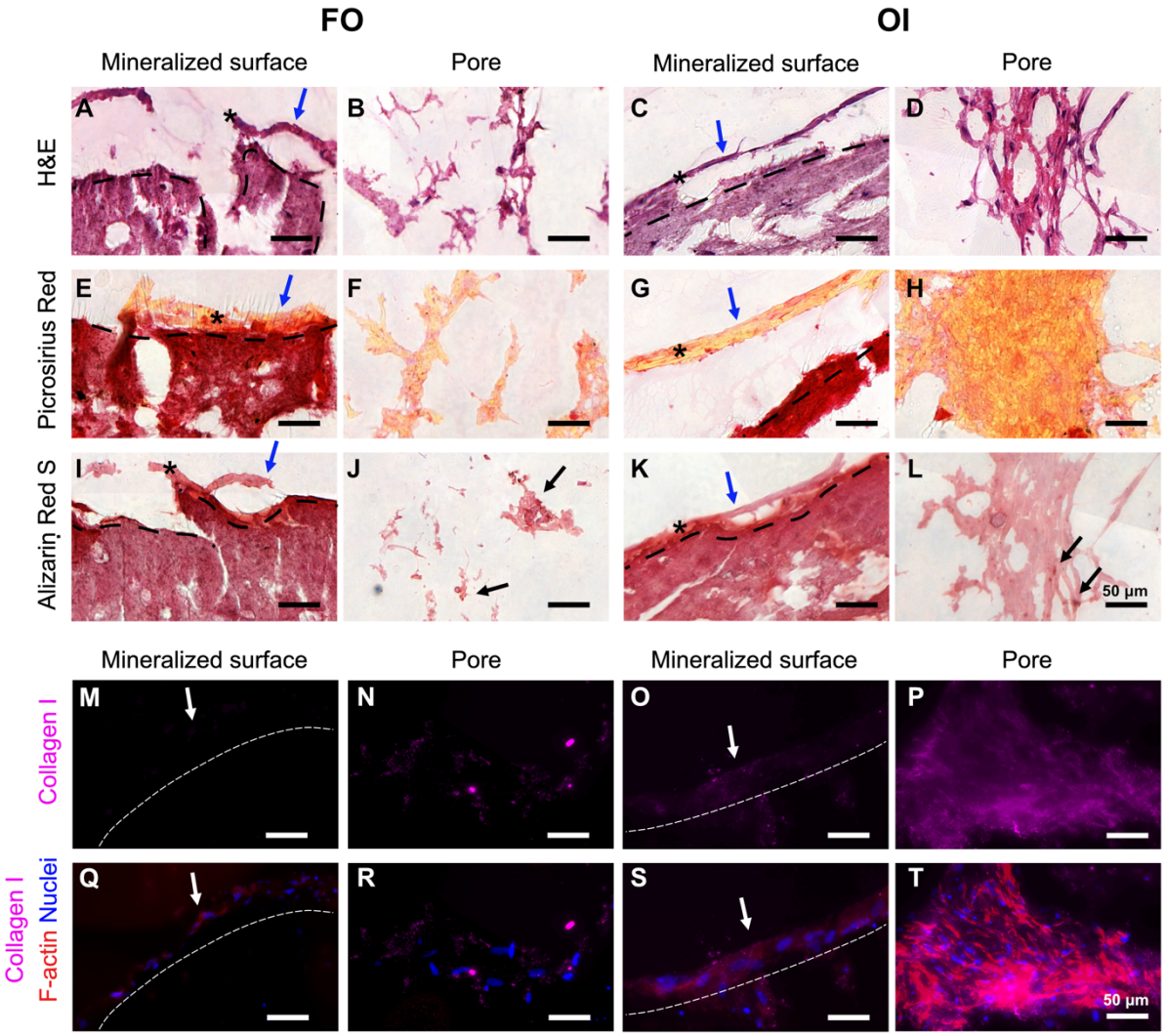

Fig. 4. Extracellular matrix characterization of patient phenotype in organotypic bone models. After 8 weeks of compression loading, consecutive sections of FO and OI organotypic bone models were stained to visualize cell and extracellular matrix morphologies in the same region. (A-L) Histological staining of hydrogel interface and pore regions in FO and OI patient organotypic bone models. Mineralized cell-laden scaffold surfaces are indicated by dotted lines, newly formed mineralized areas and surface lining cells are indicated by blue arrows. Macroscale scaffold pore regions were selected without any scaffold regions to highlight morphological differences in newly synthesized extracellular matrix compared to mineralized hydrogel scaffolds. (A-D) Haematoxylin and eosin (H&E) staining shows morphology and localization of cells. Scale bar = 50 µm. (E-H) Picrosirius red staining shows collagen (red-orange) on the construct surface and spanning across pores. Scale bar = 50 µm. (I-L) Alizarin S red staining shows cell-secreted collagenous extracellular matrix is mineralized; mineral nodules are indicated by arrows. Scale bar = 50 µm. (M-T) Immunofluorescent staining of cell nuclei (blue), F-actin (red) and collagen I (pink) shows cell-secreted collagen recapitulates woven bone and surface modelling phenotypes. Scale bar = 50 µm.

2.5 Transcriptomic profiling reveals effects of Dickkopf-1 antibody on a molecular level in organotypic bone models

To gain insight into the molecular properties of the organotypic bone models, we performed RNA sequencing (RNA-seq) analysis. Principal component analysis (PCA) of the top 1000 most variable genes demonstrated a clear separation between sample groups, with the first principal component (PC1) explaining 86% of the variance and the second principal component (PC2) accounting for an additional 9% (Fig. 5A). This substantial separation along PC1

primarily distinguished samples based on patient origin (FO versus OI), while PC2 further separated samples based on treatment status. Notably, the gene expression profiles of DKK1Ab-treated and untreated OI organotypic bone models exhibited greater similarity to each other than to those of FO models, regardless of treatment, indicating that patient-specific differences had a stronger impact on transcriptomic profiles than treatment effects. Differential expression analysis revealed substantial differences between patient groups, with 5,222 differentially expressed genes (DEGs) identified when comparing OI and FO control models (2,883 upregulated, 2,339 downregulated; Fig. 5B). Key bone-related genes including DMP1, IBSP, DKK2, ALPL, and SPP1 were significantly upregulated in OI samples compared to FO controls, while the OI-causative gene FKBP10 showed differential expression, confirming the disease phenotype at the molecular level (Figure 5B).

To unravel the biological relevance of the RNA-seq dataset, we performed Generally Applicable Gene-set Enrichment for Pathway Analysis (GAGE). Altogether, 43 gene sets displayed significant levels of upregulation in OI constructs with IgG control versus FO + IgG (q-value < 0.05). Representation of the significant upregulated gene sets in OI + IgG versus FO + IgG (Figure 5F) showed an enrichment of pathways related to extracellular matrix organization, collagen formation, focal adhesion, Wnt signalling and regulators of bone mineralization. Genes involved in bone mineralization (DMP1, SPP1 (Osteopontin), ALPL, BMP4, IBSP) were upregulated in OI + IgG versus FO + IgG control.[28] No significantly upregulated pathways were found in OI models following DKK1Ab treatment compared to IgG control.

Treatment with DKK1Ab elicited distinct transcriptional responses in FO and OI models. In FO models, DKK1Ab treatment induced significant changes in 2,278 genes (1,384 upregulated, 794 downregulated; Fig. 5C), primarily associated with extracellular matrix organization, collagen formation, and bone mineralization regulation (Figure 5G). In contrast, OI models responded to DKK1Ab treatment with altered expression of 20 genes (1 upregulated, 19 downregulated; Fig. 5D). Heatmaps of DEGs across comparison groups yielded distinct expression patterns that clearly separated samples by both patient origin and treatment status (Figure 5E). This pattern further supports the observation that while treatment with DKK1Ab induced transcriptomic changes in both FO and OI models, these changes were markedly different between patient groups, highlighting the importance of patient-specific factors in treatment response.

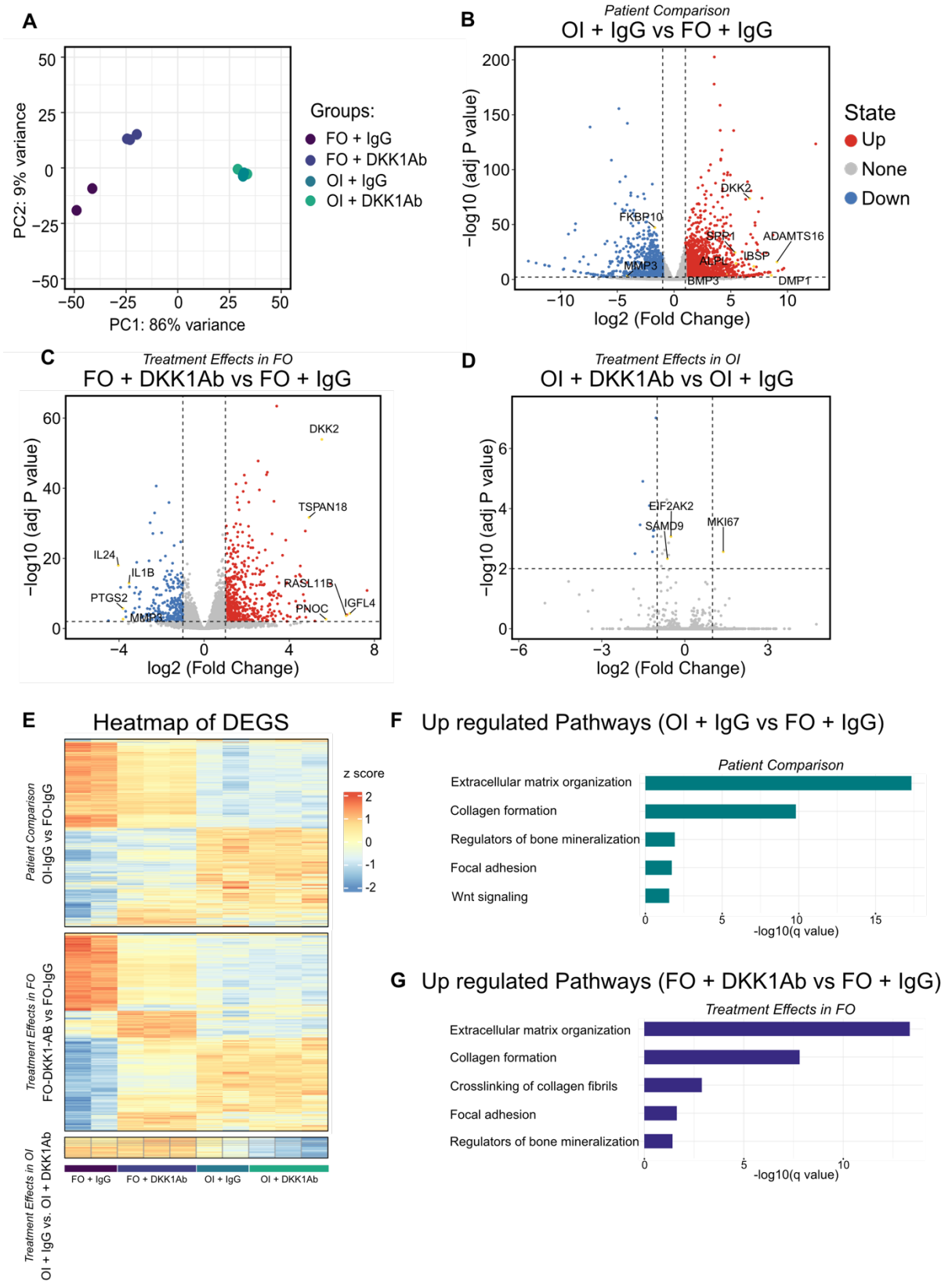

Fig. 5. Transcriptomic analyses of organotypic bone models. (A) Principal component analysis of RNA-sequencing data based on the top 1,000 most variable genes across samples showing distinct clustering of samples by patient origin (FO versus OI) and treatment (DKK1Ab versus IgG control). PC1 (86% variance) primarily separates samples by patient origin, while PC2 (9% variance) further distinguishes treatment groups. (B) Volcano plot showing differentially expressed genes between OI+IgG and FO+IgG control models, (C) Volcano plot displaying differentially expressed genes in FO models following DKK1Ab treatment compared to IgG control. (D) Volcano plot showing differentially expressed genes in OI models following DKK1Ab treatment compared to IgG control organotypic bone samples identified by RNA-seq. FDR-adjusted P value < 0.01. (E) Heatmap

illustration of gene expression values for differentially expressed genes in organotypic bone model groups. The colour gradient represents the z-score of $\log_2$ normalized counts, measured in counts per million (CPM). Red indicates a high positive z-score, indicating significantly higher expression levels; blue indicates a high negative z-score, indicating significantly lower expression levels. (F) Top upregulated pathways in OI+IgG versus FO+IgG comparison based on gene set enrichment analysis (GSEA). (G) Top upregulated pathways in FO models following DKK1Ab treatment compared to IgG control. No significantly upregulated pathways were found in OI models following DKK1Ab treatment compared to IgG control. Highlighted genes in volcano plots (B, C, D) represent key differentially expressed genes of biological significance.

2.6 Collagen expression, secretion, and deposition in organotypic bone models.

To further investigate the effects of DKK1Ab treatment on bone matrix composition, we analysed collagen expression, secretion and deposition in both FO and OI organotypic bone models. Gene expression profiling revealed distinct patterns between FO and OI models, as well as treatment-dependent alterations (Fig. 6A). Notably, genes involved in collagen synthesis (*COL1A1, COL1A2, BMP1*) and mineralization (*DMP1, SPP1, BMP4*) were upregulated in both OI groups compared to FO IgG controls.[29,30] Following DKK1Ab treatment, genes related to collagen synthesis were upregulated in FO organotypic bone models but remained unchanged in OI models, suggesting a differential regulatory effect.

To validate these transcriptomic findings at the protein level, collagen I deposition was assessed via immunohistochemical staining at endpoint to visualize extracellular matrix organization (Fig. 6B-E). FO control models showed moderate collagen I staining with fibres organized primarily along mineralized filament surfaces (Fig. 6B), while DKK1Ab treatment resulted in more intense and abundant collagen I deposition throughout the construct pores (Fig. 6C). OI models displayed dense collagen I networks in both treatment conditions (Fig. 6D, E). Quantification of collagen I fluorescence area fraction (Fig. 6F) confirmed significantly higher collagen signal in the pores of both treated and untreated OI models compared to FO + IgG. Following DKK1Ab treatment, collagen I deposition significantly increased in FO models, approaching levels seen in OI models.

To assess the dynamics of collagen secretion, we measured procollagen I levels in cell culture medium collected two days post-treatment with 1 μg/mL DKK1Ab or 1 μg/mL IgG isotype control (Fig. 6G). OI organotypic bone models exhibited higher procollagen I levels compared to FO models, reflecting the characteristic decrease in collagen crosslinking and reduced deposition into the ECM seen in FKBP10-related OI, leading to accumulation in the culture media.[31] Treatment with DKK1Ab increased early procollagen I secretion, suggesting enhanced matrix production. Notably, OI + DKK1Ab models exhibited the highest procollagen I secretion among all groups ($p<0.0001$ compared to FO + IgG), indicating that DKK1Ab treatment further enhanced the collagen production in OI models.

Collectively, these results demonstrate that DKK1Ab treatment modulates gene expression and

significantly increases collagen deposition in organotypic bone models, with effects more pronounced in the early secretion phase for OI models and in the accumulated matrix for FO models.

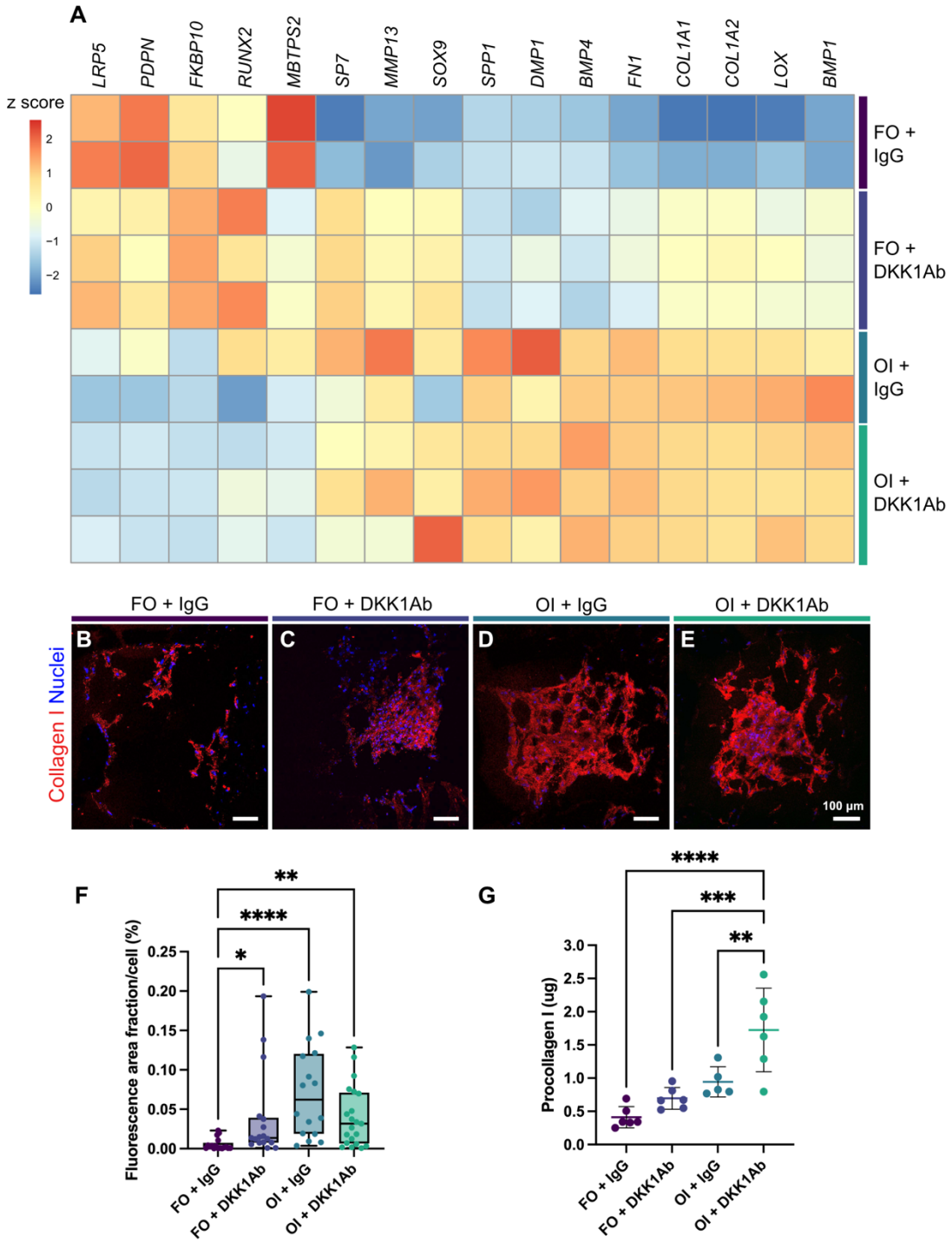

Fig. 6. Collagen and mineral related gene expression and deposition in organotypic bone models. (A) Heatmap depicting average gene expression related to collagen synthesis and mineralization in organotypic bone model groups: FO + IgG isotype control, FO + DKK1Ab treated, OI + IgG isotype control and OI + DKK1Ab treated. The colour gradient represents the z-score of $\log_2$ normalized counts, measured in counts per million (CPM). Red indicates a high positive z-score, indicating significantly higher expression levels, blue indicates high negative z-score, indicating significantly lower expression levels. (B-E) Representative immunohistochemical images of collagen I (red) showing cell-secreted collagen in macroscale pores of cryosections of 3D bioprinted organotypic

bone models. (B) FO + IgG control showing moderate collagen I staining with fibres organized along mineralized filament surfaces; (C) FO + DKK1Ab showing enhanced collagen I deposition; (D) OI + IgG control exhibiting dense collagen networks; (E) OI + DKK1Ab displaying similar collagen arrangement. Nuclei are counterstained in blue. Scale bar = 100 µm. (F) Quantification of collagen I fluorescence area fraction normalized to cell number. Statistical significance among groups was determined using the Kruskal-Wallis test followed by Dunn's post-hoc correction, * $p<0.05$, ** $p<0.01$, ****$p<0.0001$. (G) Quantification of procollagen I secretion measured by ELISA of cell culture medium taken 2 days after starting treatment in mechanically loaded FO and OI organotypic bone models. Statistical significance among groups was identified by one-way ANOVA with Tukey's multiple comparisons tests ** $p<0.01$, *** $p<0.001$, **** $p<0.0001$. DKK1Ab treatment significantly increased early procollagen I secretion in OI models while significantly increasing endpoint collagen deposition measured in FO models.

3 Discussion

This study demonstrates the successful development of a mechanically stimulated 3D bioprinted organotypic bone model that replicates key characteristics of native bone tissue and enables patient-specific response assessment to osteoanabolic treatment. The integration of primary osteoblasts derived from both metabolically healthy and FKBP10-related OI patients into an osteogenic bioink, coupled with mechanical stimulation, provides valuable insights into the pathophysiology of osteogenesis imperfecta and potential therapeutic strategies.

Developing effective treatments for rare diseases such as OI remain a significant challenge due to the complex pathophysiology, genetic heterogeneity, and limitations of *in vivo* disease models. Considering the diverse manifestations of OI, robust organotypic models are crucial for screening potential therapies and elucidating disease mechanisms in a controlled environment.[11,32] Our model addresses this need by providing a patient-specific, mechanically stimulated platform that replicates key aspects of bone structure and function.

By incorporating 3D bioprinted patient-derived osteoblasts cultured under cyclic compressive loading and reseeding mineralized surfaces with fresh osteoblasts, our method mimics aspects of woven bone formation, apposition on existing mineralized surfaces, and mineral maturation. Building upon the work of Akiva et al,[33] who demonstrated the differentiation of human MSCs into osteoblasts and osteocytes with subsequent ECM production in early-stage bone models, our approach advances the field[34] by integrating 3D bioprinted, patient-derived osteoblasts subjected to cyclic compressive loading and subsequent reseeding onto mineralized substrates, effectively recapitulating key features of woven bone formation, surface apposition, and mineral maturation.

Histological analysis revealed distinct cellular distributions, including cells embedded within the mineralized hydrogel, cells spanning across construct pores, and cells lining mineralized surfaces. Cells embedded within the hydrogel experienced direct interaction with cyclic compressive loading, potentially influencing cell-matrix interactions and collagen deposition.[13,35] However, limited peri-cellular collagen was observed in these regions, similar

to previous findings using patient-derived osteoblasts.[12] Conversely, top-seeded osteoblasts aligned along mineralized bioprinted struts and produced fibres of collagenous extracellular matrix (ECM) forming a parallel layer on the existing mineralized surface, mimicking lamellar-like bone formation[36] Moreover, reseeded osteoblasts stretched across construct pores, leading to dense collagenous matrices resembling woven bone, similar to previous reports using hMSCs seeded onto polymer scaffolds.[33,36,37]

We observed distinct differences between OI and FO organotypic models across molecular, protein, and bulk scales. OI samples exhibited over 5,000 differentially expressed genes, consistent with previous studies sequencing OI patient cells.[38,39] Notably, OI samples showed elevated *COL1A1* and *COL1A2* expression, significantly higher procollagen I levels in the cell culture medium as well as more protein deposited in the ECM compared to FO controls. The finding is consistent with the immunostaining pattern of the bone explants (Fig. S1), due to distinct differences in collagen organization and distribution in OI and FO bone. Due to the design of the 3D bioprinted scaffolds, the reseeded cells may experience macromolecular crowding within construct pores,[40] trapping newly synthesized ECM in the pore. Additionally, we observed differences in cell distribution and morphology in the OI and FO constructs, which influence ECM production,[41] where cells in FO constructs were found to line mineralized surfaces, adopting flattened morphologies mimicking lining cells, while cells in OI constructs spanned construct pores, adopting dendritic osteoblastic morphologies. Overall, collagen differences may be the result of intrinsic patient-specific variations,[42–44] local surface topography[45,46] and morphology.[47]

Mineral formation rates and mineral density increased in OI organotypic bone models, reflecting the hypermineralization phenotype of OI bone.[48] The presence of smaller mineral nodules in alizarin red stained OI sections and higher expression of SPP1 (Osteopontin) and DMP1 (Dentin Matrix Acidic Phosphoprotein 1) suggest that OI cells regulate mineral formation differently from FO controls,[28] corroborating work by Blouin et al.,[49] who demonstrated altered mineral crystal size and orientation in OI bone samples.

Time-lapsed micro-CT imaging during culture revealed hypermineralization and deformations in OI organotypic bone models compared to metabolically healthy models, recapitulating aspects of the clinical disease phenotype. Despite loss of scaffold fidelity causing large volumes of mineralized samples to deform and break off, stiffness was not statistically different in OI samples. This unexpected finding suggests complex mechanical adaptations within the OI constructs that warrant further investigation.

The differential response to DKK1Ab treatment between OI and FO samples underscores

potential dysregulations in Wnt pathway modulation for FKBP10-related OI patients. Despite increased early procollagen secretion following DKK1Ab treatment in OI samples, endpoint immunostaining of collagen and gene expression levels remained similar in treated and untreated OI organotypic bone models. Increased secretion of procollagen without increased deposition is potentially attributable to reduced collagen crosslinking characteristic of *FKBP10*-related OI,[31]. The currently available therapeutic approaches for OI aim to reduce fracture incidence by increasing bone mass. However, they do not address the underlying matrix defect, impacting the efficacy of osteoanabolic treatments in OI.

DKK1Ab treatment neutralizes DKK1, thereby allowing Wnt ligands to bind to their receptors, LRP5/6, and enhancing Wnt signaling activity.[22,50] Transcriptomic analyses did not demonstrate significant upregulation of Wnt signaling in response to DKK1Ab treatment. However, untreated OI samples exhibited enhanced Wnt signalling and decreased expression of LRP5/6 receptors compared to untreated FO models, indicating inherent differences in baseline Wnt pathway modulation between metabolically healthy and OI individuals.[50]

Within newly synthesized collagenous matrices, we observed differences in mineral nodule distribution between OI and FO models. Further exploration of surface mineralization in time-lapsed micro-CT scans[51] revealed increased surface mineralization in FO anti-DKK1 treated samples, while highlighting heterogeneous pore size distribution in OI samples resulting from fractures and construct deformations

The differential response to DKK1Ab treatment between OI and FO samples may be explained by variations in the baseline expression and regulation of the Wnt signaling pathway. While we did not directly quantify DKK1 levels in this study, our transcriptomic data revealed important insights into potential mechanisms. Notably, SP7/Osterix (OSX), which typically co-expresses with DKK1, showed divergent expression patterns between OI and FO models following treatment. In FO samples, OSX expression increased with DKK1Ab treatment, whereas OI samples exhibited a decrease in OSX expression. This inverse pattern suggests that there may be significantly less DKK1 available for antibody binding in OI cells compared to healthy osteoblasts, potentially explaining the reduced efficacy of DKK1Ab in OI organotypic bone models. Previous studies support this hypothesis, demonstrating that OSX activates DKK1 expression and that DKK1 expression is down-regulated in the absence of OSX.[52,53] This disruption in the OSX-DKK1 regulatory axis may contribute to the altered Wnt signaling dynamics observed in OI samples and limit the therapeutic potential of DKK1 inhibition in certain OI subtypes.

The ratio of woven bone and lamellar bone conformations varies between lethal (type II),

moderate, progressively deforming (type III, IV), and mild OI (type I).[54] This exploratory study used bone cells from one patient and investigated a single treatment concentration, which cannot fully capture OI heterogeneity or treatment variability across patient populations. Using cells from different OI patients, our model could investigate pathomechanisms in woven bone formation. Future studies should include multiple patients with diverse OI mutations and explore various treatment concentrations and types, driving towards a personalized medicine platform for OI.[32,55]

Several technical limitations should be acknowledged. RNA sequencing was based on expression profiles of n=2 or n=3 samples, offering exploratory views into transcriptomic differences between OI and FO samples. To elucidate functional implications of these gene expression alterations, results could be validated using RT-qPCR, ELISA, and immunostaining.[56] Our investigations suggest that the extracellular matrix plays a crucial role in the formation and maturation of organotypic bone models, consistent with emerging evidence on matrix properties directing cellular behaviour.[57] A thorough analysis is required to understand the signaling pathways involved and their roles in model development, potentially leading to more effective therapeutic strategies for OI and other skeletal disorders.

Alternative therapeutic approaches might be more effective for FKBP10-related OI. Recent studies[58–60] have shown that 4-Phenylbutyric acid (4-PBA) treatment reduces endoplasmic reticulum stress and improves collagen folding in cells from OI patients with collagen type I mutations, suggesting its potential as a complementary approach for patients with protein folding defects.

4 Conclusion

Our patient-derived organotypic bone model represents a significant advancement in precision medicine for skeletal disorders. The model utilizes patients' autologous cells to maintain intrinsic cellular characteristics while recapitulating both woven bone and surface-driven lamellar-like bone formation in a mechanically loaded, physiological system. Through multimodal analysis including time-lapsed micro-CT, transcriptomics, and immunohistochemistry, we demonstrated the model's ability to capture key differences between metabolically healthy and osteogenesis imperfecta bone, including hypermineralization and increased fragility in OI constructs.

The differential response to anti-Dickkopf-1 antibody treatment highlights the value of our model beyond genetic sequencing alone for predicting individualized treatment outcomes. This

functional assay approach provides insights into patient-specific cellular responses to mechanical and biochemical stimuli, enabling more accurate prediction of treatment efficacy. By integrating cellular-level observations with tissue-level properties, our platform establishes a foundation for transforming orthopaedic care from reactive fracture management to proactive, personalized intervention strategies for rare skeletal disorders.

Overall, this advanced organotypic bone model represents a significant step toward precision medicine in rare skeletal disorders. The potential impact extends beyond clinical outcomes to health economic benefits for traditionally underserved patients with rare conditions.[61] Similar to how mini-gut organoids transformed cystic fibrosis treatment in the Netherlands[62]—where in vitro models are now integrated into clinical workflows and supported by insurance[63,64]—our platform could establish a new paradigm for OI care. By integrating patient-specific cells, mechanical stimulation, and comprehensive analytical approaches, our model enables the evaluation of targeted therapies in a physiologically relevant environment. This approach is fuelled by the recent FDA initiative to replace animal testing in drug development, particularly for monoclonal antibodies, with more effective, human-relevant methods. The FDA's groundbreaking April 2025 announcement specifically encourages the use of human-based laboratory models that can better predict real-world outcomes and accelerate the development of novel treatments.[1] Beyond advancing our understanding of OI pathophysiology, this model establishes a template for personalized medicine approaches in rare genetic bone diseases, potentially shifting orthopaedic care from reactive fracture management to proactive, individualized intervention strategies.

5 Experimental Section

Patient-derived osteoblast isolation

Bone explants were collected from a 3-year-old female with type XI OI (FKBP10 c.890_897dup (p.Gly300Ter)) during an intermedullary rodding surgery and from a metabolically healthy 15-year-old male undergoing a femur osteotomy (FO) to correct limb malalignment under the approved study protocol by Swiss Ethics. The bone explants were collected in Dulbecco's Modified Eagle Medium (DMEM, Gibco), rinsed in Phosphate Buffered Saline (PBS, Gibco), and vortexed three times in fresh PBS to remove blood. Osteoblasts were isolated based on tissue culture plastic adherence as described previously.[12] Cells were expanded in DMEM supplemented with 10 % fetal bovine serum (FBS, Gibco), and 1 % antibiotic-antimycotic (Gibco, 100 U/ml penicillin, 100 mg/ml streptomycin, 0.25 mg/ml

Amphotericin B), and cryopreserved in FBS and 10 % dimethyl sulfoxide (DMSO).

Bone preparation

Segments of bone explants were also prepared for sectioning. After washing in PBS, segments of the bone explants were fixed in 4 % paraformaldehyde (PFA) for 48 hr, washed three times in PBS and decalcified in 12.5 % EDTA (pH 7.4–7.6) for 1-2 weeks at 4 °C (decalcification confirmed by scout view in microCT40 (SCANCO Medical AG, Brüttisellen, Switzerland)). Demineralized bone was then dehydrated in 20 % sucrose and 2 % Polyvinylpyrrolidone (PVP) for 3 days, followed by 30 % sucrose and 2 % PVP solution for 2 weeks. Bones were embedded in optimal cutting temperature compound (OCT, VWR) and flash frozen in liquid nitrogen. Cryosections (10–50 µm thickness) were prepared using Kawamoto's cryofilm type 2C (SECTION-LAB Co. Ltd., Japan).[65]

Bioink preparation and 3D bioprinting

Primary patient-derived osteoblasts were harvested and combined with hydrogels comprising 4.1 % (w/v) gelatine, 0.8 % (w/v) alginate, and 0.1 % (w/v) graphene oxide to form osteogenic bioinks with a concentration of $10x10^6$ cells/mL, as described previously.[12,66] The bioinks were extrusion bioprinted using a 3DDiscovery bioprinter (RegenHU; Villaz-St-Pierre, Switzerland) equipped with a pneumatic dispenser. The lattice structures were printed directly onto double-sided tape (3M, Saint Paul, USA) secured on bioreactor platforms, following established procedures.[13] Directly after bioprinting, samples were crosslinked in 2 % (w/v) calcium chloride in control medium (DMEM, 10 % FBS, 1% antibiotic-antimycotic) for 10 minutes. Samples were washed twice in control medium and incubated (37 °C, 5 % CO_2) overnight at before being assembled into compression bioreactors.

Organotypic bone intervention study

Metabolically healthy and *FKBP10*-OI (homozygous for FKBP10 c.890_897dup; p.Gly300Ter) cell-laden scaffolds were individually housed in custom bioreactors and subjected to uniaxial compressive loading three times per week in a mechanical stimulation unit (MSU). Each bioreactor was filled with 5 mL differentiation medium (DMEM, 10 % FBS, 1 % Anti-Anti, 50 µg/mL ascorbic acid, 10 mM β-glycerophosphate, 100 nM dexamethasone) and incubated at 37 °C and 5 % CO_2 with media changes performed three times per week. Samples received fixed loading three times per week with a 0.07N preload to define the sample contact position with the bioreactor piston, followed by a sinusoidal strain amplitude of 1% at a

frequency of 5 Hz for 300 seconds. Once per week medium was collected and bioreactors were scanned by micro-CT as described previously.[12] After a preculture period of 4 weeks, 1 million fresh osteoblasts were pipetted onto each construct. After reseeding, samples received growth medium (DMEM, 10 % FBS, 1 % Anti-Anti, 50 µg/mL ascorbic acid, 10 mM β-glycerophosphate) supplemented with 1 µg/mL Dickkopf-1 antibody (treatment group) (R&D Systems AF1096) or 1 µg/mL Goat IgG (control group) (R&D Systems AF1096). Thereafter, to adapt to increased sample stiffness, the loading regimen was adjusted to an adaptive loading protocol (0.05 N preload, displacement-controlled position to 10 % strain, 1 % sinusoidal strain at 5 Hz for 500 seconds) for the final four weeks of culture.

Time-lapsed micro-computed tomography

Mineralization was monitored by *in situ* time-lapsed micro-CT scanning as described previously. [12] Each bioreactor was scanned every 7 days in a micro-CT scanner (µCT45, SCANCO Medical AG, Brüttisellen, Switzerland) with a voxel resolution of 34.5 µm. The bioreactors were scanned at 45 kVp and 177 µA intensity with a 600 ms integration time.

Image processing

Image processing was performed using an in-house software framework based on Python 3.6.6 (Python Software Foundation, Delaware). Time-lapsed micro-CT images were registered to the first time point for each sample. A consistent volume of interest was established by defining a mask around samples. To diminish image noise, a constrained Gaussian filter (with sigma 1.2 and support 3) was applied using IPL Scanco AG software V5.42. For segmentation of mineralized samples from the background, a global threshold of 74 mg HA/cm^3 was applied. Mineral volume and density measurements were calculated from segmented greyscale images. Mineral formation rate was calculated by subtracting the mineral volume from the previous week. Samples that were broken were excluded from analysis. 3D visualizations were performed using ParaView 5.4.0 (Kitware, Clifton Park, New York).[67]

To quantify lost volume from fractures, surface mineral formation in the bone model, we implemented a rigorous image processing pipeline similar to those described previously.[37,68] The grayscale intensity images from the follow-up timepoints were registered to the images from day 28. These images were then Gaussian filtered (sigma = 1, support 1.2) to reduce noise and thresholded at 74 mg HA/cm³. Then an additional Gaussian filter with sigma = 3 and support 3) was applied using Python 3.11.6 and SciPy 1.15.0, followed by binarization with the threshold that was determined with Otsu (Scikit-Image 0.24.0) for day 28. This approach

allowed us to define an envelope that tightly encloses the filament structure of the bone model. To define a precise volume of interest, the binary masks underwent a series of morphological operations. First, holes within each XY plane were filled to ensure continuity of the structure. The masks were then dilated by 20 iterations to encompass nearby features, followed by an erosion of 21 iterations to create a tight-fitting boundary around the structure. Additional hole-filling was performed similarly in the other planes (XZ, YZ) to generate a fully enclosed 3D envelope. This processing was performed for each time point individually, allowing consistent volumetric analysis across the experimental timeline. Morphological operations were implemented using NumPy 1.26.4 and SciPy's ndimage.

Deformed volumes, stable regions and lost volumes were calculated by performing binary volume comparison on the time-lapsed image. A region that was stable across all time points was calculated from the union of the envelopes from all time points. In combination with the previously filamentous object, a negative mask was calculated representing the pores and voids of the bone model. Pore spaces were calculated according to methods described by van Lenthe et al.,[51] with PoreSpy 2.4.2. The normalized reduction in pore space was assessed by calculating the mean pore size at each time point. Overall, this process enabled a quantitative assessment of structural changes throughout the experimental timeline.

Scaffold mechanics

Scaffold mechanics were assessed using the in-house MSU as following established procedures.[12,13,37] Briefly, non-destructive measurements were acquired during the loading protocol. At endpoint, unconfined uniaxial compression tests were conducted under displacement control, applying a preload of 0.05 N to determine sample height and contact position, returning to baseline and then compressing with a displacement rate of 4 μm/s until the scaffold reached its yield point. During compression, both force and displacement were recorded and subsequently analysed using Python software (Python Software Foundation, Delaware, USA). The stiffness of the scaffold was derived from the fitted curve, calculated as the ratio of force to displacement at the steepest slope within the linear elastic range as described previously.[13]

Sandwich ELISA assay

Procollagen Type I concentration was assessed in the cell culture supernatant using the Human Pro-Collagen I alpha I matched antibody pair kit (ab216064, Abcam) and ELISA accessory pack (ab210905, Abcam) according to the manufacturer’s instructions. The optical density was

determined after 5 minutes of incubation with TMD Substrate (ab210902, Abcam) at 600 nm using a plate reader (Tecan Spark 10 M, Männedorf, Switzerland). Procollagen I concentrations were calculated from the collagen standard curves using GraphPad Prism 10.

RNA Extraction, High Throughput Sequencing and Analysis

At endpoint, cell-laden scaffolds were washed thrice in PBS and removed from compression bioreactors. Constructs were homogenized in Trizol Reagent (Invitrogen, Thomas Fisher Scientific, USA) with a pellet pestle motor. Chloroform was added to induce phase separation and the clear aqueous phase was transferred to an RNeasy Micro Kit spin column (Qiagen, Switzerland) to isolate total RNA according to the manufacturer's instructions. As exploratory study, RNA sequencing was performed on n=2 IgG control samples and n=3 anti-DKK1 treated samples. RNA integrity was assessed using a 2100 BioAnalyzer from Agilent. Sequencing libraries were prepared with the TruSeq Stranded Total RNA Library Prep Kit from Illumina, following the manufacturer's protocol. Paired-end sequencing was performed on all samples at the Functional Genomics Center in Zurich.

Raw sequence data quality was evaluated using FastQC (Version: FastQC v0.11.9, http://www.bioinformatics.babraham.ac.uk/projects/fastqc/). The raw reads were mapped to the human reference genome using subread (Version 2.0.1).[69] The human genome index was created from subread-build index. The aligned reads were quantified on a gene basis using featureCounts (Version 2.0.1).[70] RNA-sequencing data were uploaded to ArrayExpress (http://www.ebi.ac.uk/arrayexpress/) with the accession number GSE291327.
To explore the similarities and dissimilarities between the samples, the quantified count data were normalized using the Variance Stabilizing Transformation (VST) from the DESeq2 package.[70] The principal component analysis (PCA) was performed on transformed read counts using the top 1000 most variable genes to assess the overall similarity between the sample. The differentially expressed genes analysis between FO + DKK1Ab versus FO + IgG, OI + DKK1Ab versus OI + IgG, OI versus FO + IgG groups was performed using DESeq2.[71] The differentially expressed genes were selected using an FDR-adjusted P value cut-off < 0.01. The Ensemble ID was annotated to gene symbols and Entrez Gene using biomaRt (BioConductor version 3.20, R version 4.4.2) and further differentially expressed genes filtered with only protein coding genes. Lists of differentially regulated genes for the different group comparisons are provided in Supplementary Tables 1–3.
Gene-set enrichment analysis was performed using Generally Applicable Gene-set Enrichment

(GAGE) (Bioconductor, version 3.20).[72] For functional annotation of signalling pathways, we used gene sets from ConsensusPathDB.[73] The analysis was performed on the basis of one-on-one comparisons, comparing between patients OI + IgG versus FO + IgG, and effect of treatment as FO + DKK1Ab versus FO + IgG and OI + DKK1Ab versus OI + IgG, data. The significant pathways terms were selected using an FDR-adjusted P value < 0.05. Lists of enriched pathways terms in upregulated gene sets are provided in Supplementary Tables 4 and 5.

Sample preparation and histological staining

At endpoint, cell-laden scaffolds were washed twice in PBS and fixed in 4 % formaldehyde in PBS for 2 hours. Samples were washed twice and incubated in 10 % sucrose in PBS for 2 hours. Samples were incubated in 30 % sucrose in PBS overnight for cryoprotection. Subsequently, the scaffolds were embedded in optimal cutting temperature compound (OCT, VWR) and frozen in a methanol bath on dry ice. Samples were sectioned using Kawamoto's cryofilm type 2C (SECTION-LAB Co. Ltd., Japan) on a cryotome (CryoStar NX70, Thermo Scientific).[65] Prior to staining, 10-30 µm sections were affixed to microscope slides (SuperFrost™ Microscope Slides, ThermoScientific) using a solution of 1 % (w/v) chitosan in 1 % (v/v) acetic acid. Staining procedures included haematoxylin and eosin (H&E) staining to visualize cell nuclei, cytoplasm, and extracellular matrix, Alizarin Red S staining (2 mg/mL in acetone pH 4.3) (A5533, Sigma-Aldrich) to highlight mineralized extracellular matrix, and Picrosirius red staining (365548, P6744, Sigma-Aldrich) for collagen visualization. Imaging of the histological sections was conducted using an automated slide scanner (Panoramic 250 Flash II, 3Dhistech, Hungary) at ×20 magnification.

Collagen I protein was analysed by immunohistochemical staining. Briefly, 30 µm cryosections were washed thrice in PBS, followed by permeabilization in 0.1 % Triton-X-100 in PBS for 20 minutes. Subsequently, sections were washed again in PBS three times and blocked in 3 % BSA in PBS for 1 hour. Sections were incubated overnight at 4 °C with primary anti-collagen I antibody (1:200, ab6308, Abcam) in 1 % BSA in PBS. Control sections were incubated with mouse IgG isotype control (1:200, 026502, Invitrogen) overnight at 4 °C. Sections were washed thrice and incubated with secondary donkey anti-mouse Alexa Fluor 647 (ab150107, Abcam) for 1 hour. Sections were washed thrice in PBS and incubated with Alexa Fluor Plus 555 Phalloidin (1:500, A30106, Invitrogen) for 1 hour. Sections were washed thrice and incubated with Hoechst 33342 (1:200, B2261, Sigma Aldrich) for 20 mins. Sections were washed thrice in PBS, mounted with ProLong Gold Antifade Mountant (P10144, Invitrogen), and sealed with

nail polish. Imaging was performed using a Leica TCS SP8 confocal microscope (Leica Microsystems, Heerbrugg, Switzerland) and an automated slide scanner (Panoramic 250 Flash II, 3Dhistech, Hungary) at 40× magnification. Cell density (cells/mm^2) was determined from Hoechst-stained nuclei automatically using ImageJ software. Similarly, fluorescence area fraction (%) in collagen I immunostained cryosections was evaluated using automatic Otsu thresholding in ImageJ.

Statistical analysis

Statistical analysis was performed using GraphPad Prism 10 or R 4.2.2 with the tidyverse, lme4, and lmerTest packages. *p-values less than 0.05 were considered statistically significant. Time-lapse data were analysed using two-way ANOVA followed by Tukey's multiple comparisons test. Group comparisons at a single time point were conducted using one-way ANOVA with post-hoc Tukey's multiple comparisons test for normally distributed data. For non-normally distributed data, groups were analysed with Kruskal-Wallis test followed by Dunn's post-hoc correction. Time-lapsed micro-CT results for lost volume and normalized pore space were analysed using linear mixed-effects models, with treatment group and timepoint as fixed effects and sample as a random effect. Statistical significance was determined using Type III ANOVA with Satterthwaite's method for denominator degrees of freedom. Post-hoc comparisons between groups were performed with Bonferroni-adjusted p-values to control for multiple testing.

Acknowledgements

This project was supported by the grant # 2022-487 of the Strategic Focal Area 'Personalized Health and Related Technologies (PHRT to GNS)' of the ETH Domain (Swiss Federal Institutes of Technology) and the Swiss National Science Foundation (SNF Project 31003A_ 207542 to CG and MRo). The authors thank the Scientific Center for Optical and Electron Microscopy (ScopeM) of ETH Zurich for their support and assistance in this work. During the preparation of this manuscript the authors used the OpenAI ChatGPT and Anthropic Claude tool to improve the readability and grammar of the manuscript.

Supporting Information

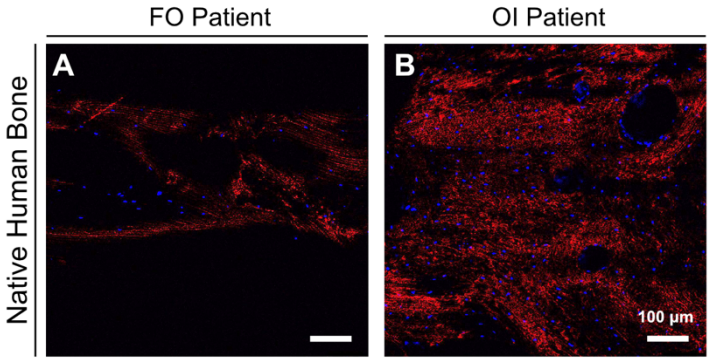

Fig. S1. Confocal imaging of collagen type I in bone sections of FO and OI patients. A) Confocal imaging of immunofluorescent staining of cell nuclei (blue) and collagen I (red) of native bone from FO and B) OI patients. Samples serve as positive controls for collagen I immunostaining, revealing distinct differences in collagen organization and distribution in OI and FO bone. Scale bar = 100 µm.

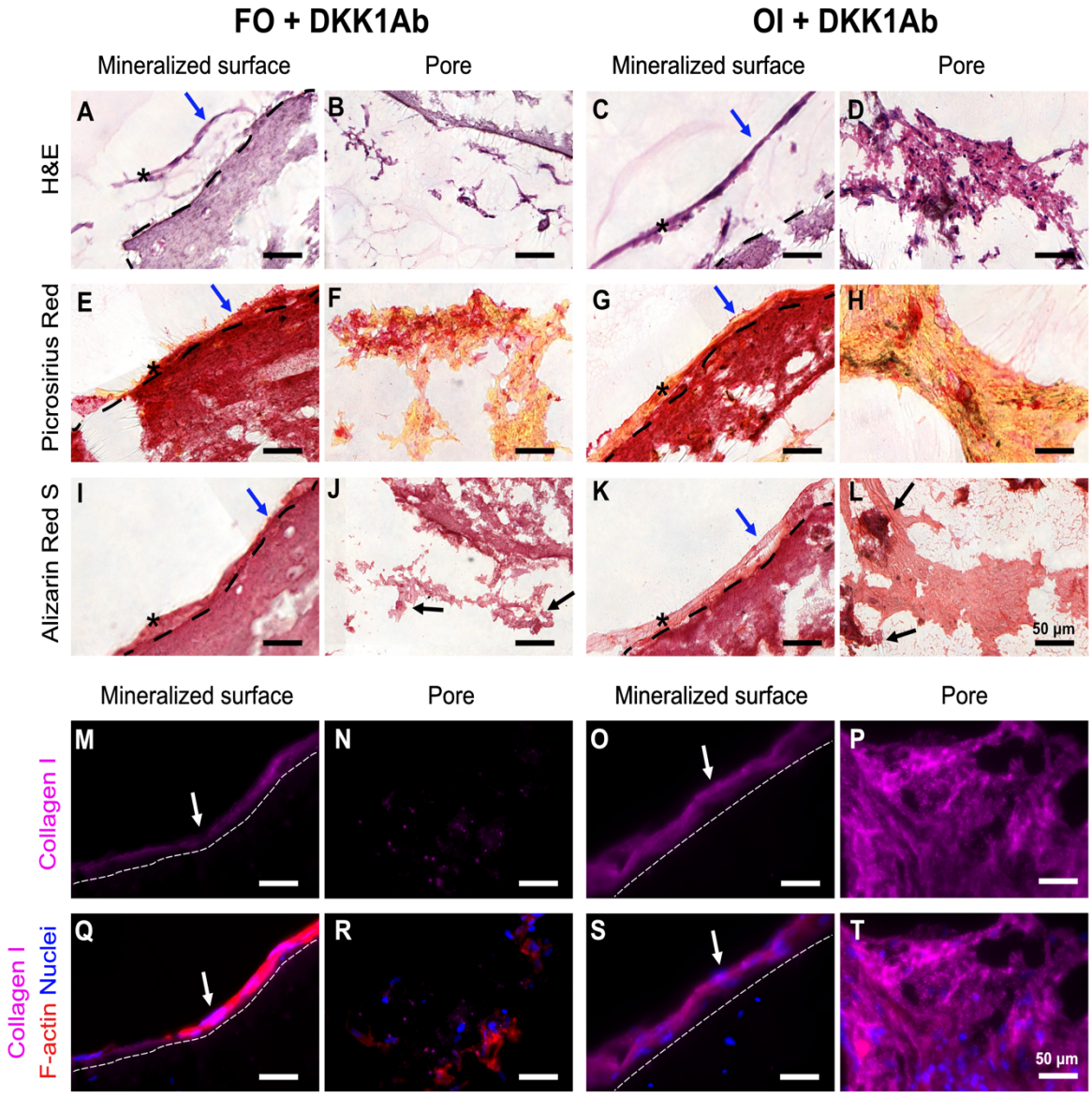

Fig. S2. Extracellular matrix characterization of patient phenotype in organotypic bone models. After 8 weeks of compression loading, consecutive sections of FO and OI organotypic bone models were stained to visualize cell and extracellular matrix morphologies in the same region. (A-L) Histological staining of hydrogel interface and pore regions in FO and OI patient organotypic bone models. Mineralized cell-laden scaffold surfaces are indicated by dotted lines, newly formed mineralized areas and surface lining cells are indicated by blue arrows. Macroscale scaffold pore regions were selected without any scaffold regions to highlight morphological differences in newly synthesized extracellular matrix compared to mineralized hydrogel scaffolds. (A-D) Hematoxylin and eosin (H&E) staining shows morphology and localization of cells. Scale bar = 50 µm. (E-H) Picrosirius red staining shows collagen (red-orange) on the construct surface and spanning across pores. Scale bar = 50 µm. (I-L) Alizarin S red staining shows cell-secreted collagenous extracellular matrix is mineralized; mineral nodules are indicated by arrows. Scale bar = 50 µm. (M-T) Immunofluorescent staining of cell nuclei (blue), F-actin (red) and collagen I (pink) shows cell-secreted collagen recapitulates woven bone and surface modelling phenotypes. Scale bar = 50 µm.

Supplementary Table S1 (ST-1.xslx): Differential gene expression (DEG) analysis of OF FO + DKK1Ab vs FO + IgG

Supplementary Table S2 (ST-2.xslx): Differential gene expression (DEG) analysis of l OI + IgG vs FO + IgG (FDR-adjusted p-value cutoff < 0.01)

Supplementary Table S3 (ST-3.xslx): Differential gene expression (DEG) analysis of OI-DKK1 vs OI-IgG (FDR-adjusted p-value cutoff < 0.01)

Supplementary Table S4 (ST-4.xslx): Gene-set enrichment analysis of up regulated pathways between FO + DKK1Ab vs FO + IgG (FDR-adjusted p value cutoff

Supplementary Table S5 (ST-4.xslx): Gene-set enrichment analysis of Upregulated pathway between OI-IgG vs LM-IgG (FDR-adjusted p-value cutoff < 0.05)

Part of the data discussed in this publication has been deposited in NCBI's Gene Expression Omnibus and is accessible through GEO Series accession number GSE291327 (https://www.ncbi.nlm.nih.gov/geo/query/acc.cgi?acc=GSE291327).

References

(1) Commissioner, O. of the. *FDA Announces Plan to Phase Out Animal Testing Requirement for Monoclonal Antibodies and Other Drugs*. FDA. https://www.fda.gov/news-events/press-announcements/fda-announces-plan-phase-out-animal-testing-requirement-monoclonal-antibodies-and-other-drugs (accessed 2025-04-17).

(2) Clevers, H. Modeling Development and Disease with Organoids. *Cell* **2016**, *165* (7), 1586–1597. https://doi.org/10.1016/j.cell.2016.05.082.

(3) Forlino, A.; Marini, J. C. Osteogenesis Imperfecta. *The Lancet* **2016**, *387* (10028), 1657–1671. https://doi.org/10.1016/s0140-6736(15)00728-x.

(4) Panzaru, M. C.; Florea, A.; Caba, L.; Gorduza, E. V. Classification of Osteogenesis Imperfecta: Importance for Prophylaxis and Genetic Counseling. *World J Clin Cases* **2023**, *11* (12), 2604–2620. https://doi.org/10.12998/wjcc.v11.i12.2604.

(5) Phillips, C. L.; Carleton, S. M.; Gentry, B. A. Animal Models of Osteogenesis Imperfecta. In *Osteogenesis Imperfecta*; 2014; pp 197–207.

(6) Lietman, C. D.; Rajagopal, A.; Homan, E. P.; Munivez, E.; Jiang, M. M.; Bertin, T. K.; Chen, Y.; Hicks, J.; Weis, M.; Eyre, D.; Lee, B.; Krakow, D. Connective Tissue Alterations in Fkbp10-/- Mice. *Hum Mol Genet* **2014**, *23* (18), 4822–4831. https://doi.org/10.1093/hmg/ddu197.

(7) Rauch, F.; Geng, Y.; Lamplugh, L.; Hekmatnejad, B.; Gaumond, M. H.; Penney, J.; Yamanaka, Y.; Moffatt, P. Crispr-Cas9 Engineered Osteogenesis Imperfecta Type V

Leads to Severe Skeletal Deformities and Perinatal Lethality in Mice. *Bone* **2018**, *107*, 131–142. https://doi.org/10.1016/j.bone.2017.11.013.

(8) Enderli, T. A.; Burtch, S. R.; Templet, J. N.; Carriero, A. Animal Models of Osteogenesis Imperfecta: Applications in Clinical Research. *Orthop Res Rev* **2016**, *8*, 41–55. https://doi.org/10.2147/ORR.S85198.

(9) Kozloff, K. M. Osteogenesis Imperfecta: A Need to Understand Divergent Treatment Outcomes in a Disorder Rich in Heterogeneity. *J Bone Min. Res* **2019**, *34* (2), 205–206. https://doi.org/10.1002/jbmr.3647.

(10) Amgen. *An Open-Label, Ascending Multiple-Dose Study to Evaluate Safety, Tolerability, Pharmacokinetics, and Pharmacodynamics of Romosozumab in Children and Adolescents With Osteogenesis Imperfecta*; Clinical trial registration NCT04545554; clinicaltrials.gov, 2023. https://clinicaltrials.gov/study/NCT04545554 (accessed 2025-04-10).

(11) Unger, S.; Ferreira, C. R.; Mortier, G. R.; Ali, H.; Bertola, D. R.; Calder, A.; Cohn, D. H.; Cormier-Daire, V.; Girisha, K. M.; Hall, C.; Krakow, D.; Makitie, O.; Mundlos, S.; Nishimura, G.; Robertson, S. P.; Savarirayan, R.; Sillence, D.; Simon, M.; Sutton, V. R.; Warman, M. L.; Superti-Furga, A. Nosology of Genetic Skeletal Disorders: 2023 Revision. *Am. J. Med. Genet. A.* **2023**, *191* (5), 1164–1209. https://doi.org/10.1002/ajmg.a.63132.

(12) de Leeuw, A. M.; Graf, R.; Lim, P. J.; Zhang, J.; Schadli, G. N.; Peterhans, S.; Rohrbach, M.; Giunta, C.; Ruger, M.; Rubert, M.; Muller, R. Physiological Cell Bioprinting Density in Human Bone-Derived Cell-Laden Scaffolds Enhances Matrix Mineralization Rate and Stiffness under Dynamic Loading. *Front Bioeng Biotechnol* **2024**, *12*, 1310289. https://doi.org/10.3389/fbioe.2024.1310289.

(13) Zhang, J.; Griesbach, J.; Ganeyev, M.; Zehnder, A.-K.; Zeng, P.; Schädli, G. N.; Leeuw, A. de; Lai, Y.; Rubert, M.; Müller, R. Long-Term Mechanical Loading Is Required for the Formation of 3D Bioprinted Functional Osteocyte Bone Organoids. *Biofabrication* **2022**, *14* (3), 035018. https://doi.org/10.1088/1758-5090/ac73b9.

(14) Walle, M.; Duseja, A.; Whittier, D. E.; Vilaca, T.; Paggiosi, M.; Eastell, R.; Müller, R.; Collins, C. J. Bone Remodeling and Responsiveness to Mechanical Stimuli in Individuals with Type 1 Diabetes Mellitus. *J. Bone Miner. Res.* **2024**, *39* (2), 85–94. https://doi.org/10.1093/jbmr/zjad014.

(15) Micha, D.; Pals, G.; Smit, T. H.; Ghazanfari, S. An in Vitro Model to Evaluate the Properties of Matrices Produced by Fibroblasts from Osteogenesis Imperfecta and Ehlers-Danlos Syndrome Patients. *Biochem Biophys Res Commun* **2019**. https://doi.org/10.1016/j.bbrc.2019.09.081.

(16) Lamande, S. R.; Ng, E. S.; Cameron, T. L.; Kung, L. H. W.; Sampurno, L.; Rowley, L.; Lilianty, J.; Patria, Y. N.; Stenta, T.; Hanssen, E.; Bell, K. M.; Saxena, R.; Stok, K. S.; Stanley, E. G.; Elefanty, A. G.; Bateman, J. F. Modeling Human Skeletal Development Using Human Pluripotent Stem Cells. *Proc Natl Acad Sci U A* **2023**, *120* (19), e2211510120. https://doi.org/10.1073/pnas.2211510120.

(17) Kawai, S.; Yoshitomi, H.; Sunaga, J.; Alev, C.; Nagata, S.; Nishio, M.; Hada, M.; Koyama, Y.; Uemura, M.; Sekiguchi, K.; Maekawa, H.; Ikeya, M.; Tamaki, S.; Jin, Y.; Harada, Y.; Fukiage, K.; Adachi, T.; Matsuda, S.; Toguchida, J. In Vitro Bone-like Nodules Generated from Patient-Derived iPSCs Recapitulate Pathological Bone Phenotypes. *Nat. Biomed. Eng.* **2019**, *3* (7), 558–570. https://doi.org/10.1038/s41551-019-0410-7.

(18) Claeys, L.; Zhytnik, L.; Ventura, L.; Wisse, L. E.; Eekhoff, E. M. W.; Pals, G.; Bravenboer, N.; Heine, V. M.; Micha, D. In Vitro Modelling of Osteogenesis Imperfecta with Patient-Derived Induced Mesenchymal Stem Cells. *Int. J. Mol. Sci.* **2024**, *25* (6). https://doi.org/10.3390/ijms25063417.

(19) Schulte, F. A.; Griesbach, J. K.; Weigt, C.; Salis-Soglio, M. von; Lambers, F. M.; Marques, F. C.; Kneissel, M.; Richards, P. J.; Kuhn, G. A.; Müller, R. Combined Physical

and Pharmaceutical Anabolic Osteoporosis Therapies Synergistically Increase Bone Response and Local Mechanoregulation. *bioRxiv* **2025**, 2024.05.16.594551. https://doi.org/10.1101/2024.05.16.594551.

(20) Ke, H. Z.; Richards, W. G.; Li, X.; Ominsky, M. S. Sclerostin and Dickkopf-1 as Therapeutic Targets in Bone Diseases. *Endocr Rev* **2012**, *33* (5), 747–783. https://doi.org/10.1210/er.2011-1060.

(21) Glorieux, F. H.; Devogelaer, J.-P.; Durigova, M.; Goemaere, S.; Hemsley, S.; Jakob, F.; Junker, U.; Ruckle, J.; Seefried, L.; Winkle, P. J. BPS804 Anti-Sclerostin Antibody in Adults With Moderate Osteogenesis Imperfecta: Results of a Randomized Phase 2a Trial. *J. Bone Miner. Res.* **2017**, *32* (7), 1496–1504. https://doi.org/10.1002/jbmr.3143.

(22) Brunetti, G.; Papadia, F.; Tummolo, A.; Fischetto, R.; Nicastro, F.; Piacente, L.; Ventura, A.; Mori, G.; Oranger, A.; Gigante, I.; Colucci, S.; Ciccarelli, M.; Grano, M.; Cavallo, L.; Delvecchio, M.; Faienza, M. F. Impaired Bone Remodeling in Children with Osteogenesis Imperfecta Treated and Untreated with Bisphosphonates: The Role of DKK1, RANKL, and TNF-α. *Osteoporos. Int.* **2016**, *27* (7), 2355–2365. https://doi.org/10.1007/s00198-016-3501-2.

(23) Florio, M.; Gunasekaran, K.; Stolina, M.; Li, X.; Liu, L.; Tipton, B.; Salimi-Moosavi, H.; Asuncion, F. J.; Li, C.; Sun, B.; Tan, H. L.; Zhang, L.; Han, C. Y.; Case, R.; Duguay, A. N.; Grisanti, M.; Stevens, J.; Pretorius, J. K.; Pacheco, E.; Jones, H.; Chen, Q.; Soriano, B. D.; Wen, J.; Heron, B.; Jacobsen, F. W.; Brisan, E.; Richards, W. G.; Ke, H. Z.; Ominsky, M. S. A Bispecific Antibody Targeting Sclerostin and DKK-1 Promotes Bone Mass Accrual and Fracture Repair. *Nat Commun* **2016**, *7*, 11505. https://doi.org/10.1038/ncomms11505.

(24) Glantschnig, H.; Hampton, R. A.; Lu, P.; Zhao, J. Z.; Vitelli, S.; Huang, L.; Haytko, P.; Cusick, T.; Ireland, C.; Jarantow, S. W.; Ernst, R.; Wei, N.; Nantermet, P.; Scott, K. R.; Fisher, J. E.; Talamo, F.; Orsatti, L.; Reszka, A. A.; Sandhu, P.; Kimmel, D.; Flores, O.; Strohl, W.; An, Z.; Wang, F. Generation and Selection of Novel Fully Human Monoclonal Antibodies That Neutralize Dickkopf-1 (DKK1) Inhibitory Function in Vitro and Increase Bone Mass in Vivo. *J Biol Chem* **2010**, *285* (51), 40135–40147. https://doi.org/10.1074/jbc.M110.166892.

(25) Brunetti, G.; Papadia, F.; Tummolo, A.; Fischetto, R.; Nicastro, F.; Piacente, L.; Ventura, A.; Mori, G.; Oranger, A.; Gigante, I.; Colucci, S.; Ciccarelli, M.; Grano, M.; Cavallo, L.; Delvecchio, M.; Faienza, M. F. Impaired Bone Remodeling in Children with Osteogenesis Imperfecta Treated and Untreated with Bisphosphonates: The Role of DKK1, RANKL, and TNF-Alpha. *Osteoporos Int* **2016**, *27* (7), 2355–2365. https://doi.org/10.1007/s00198-016-3501-2.

(26) Wang, Y.; Hu, J.; Sun, L.; Zhou, B.; Lin, X.; Zhang, Q.; Wang, O.; Jiang, Y.; Xia, W.; Xing, X.; Li, M. Correlation of Serum DKK1 Level with Skeletal Phenotype in Children with Osteogenesis Imperfecta. *J. Endocrinol. Invest.* **2024**, *47* (11), 2785–2795. https://doi.org/10.1007/s40618-024-02380-9.

(27) Ko, J.-Y.; Wang, F.-S.; Lian, W.-S.; Yang, F.-S.; Chen, J.-W.; Huang, P.-H.; Liao, C.-Y.; Kuo, S.-J. Dickkopf-1 (DKK1) Blockade Mitigates Osteogenesis Imperfecta (OI) Related Bone Disease. *Mol. Med.* **2024**, *30* (1), 66. https://doi.org/10.1186/s10020-024-00838-3.

(28) Anne George; Arthur Veis. Phosphorylated Proteins and Control over Apatite Nucleation, Crystal Growth, and Inhibition. *Chem. Rev.* **2008**, *108* (11), 4670–4693. https://doi.org/10.1021/cr0782729.

(29) Claeys, L.; Storoni, S.; Eekhoff, M.; Elting, M.; Wisse, L.; Pals, G.; Bravenboer, N.; Maugeri, A.; Micha, D. Collagen Transport and Related Pathways in Osteogenesis Imperfecta. *Hum Genet* **2021**, *140* (8), 1121–1141. https://doi.org/10.1007/s00439-021-02302-2.

(30) J. P. Gorski. Biomineralization of Bone: A Fresh View of the Roles of Non-Collagenous

Proteins. *Front. Biosci.* **2011**, *16* (7), 2598–2621. https://doi.org/10.2741/3875.
(31) Barnes, A. M.; Cabral, W. A.; Weis, M.; Makareeva, E.; Mertz, E. L.; Leikin, S.; Eyre, D.; Trujillo, C.; Marini, J. C. Absence of FKBP10 in Recessive Type XI Osteogenesis Imperfecta Leads to Diminished Collagen Cross-Linking and Reduced Collagen Deposition in Extracellular Matrix. *Hum. Mutat.* **2012**, *33* (11), 1589–1598. https://doi.org/10.1002/humu.22139.
(32) Volpato, V.; Webber, C. Addressing Variability in iPSC-Derived Models of Human Disease: Guidelines to Promote Reproducibility. *Dis. Model. Mech.* **2020**, *13* (1), dmm042317. https://doi.org/10.1242/dmm.042317.
(33) Akiva, A.; Melke, J.; Ansari, S.; Liv, N.; Meijden, R.; Erp, M.; Zhao, F.; Stout, M.; Nijhuis, W. H.; Heus, C.; Muñiz Ortera, C.; Fermie, J.; Klumperman, J.; Ito, K.; Sommerdijk, N.; Hofmann, S. An Organoid for Woven Bone. *Adv. Funct. Mater.* **2021**, *2010524*, 2010524. https://doi.org/10.1002/adfm.202010524.
(34) Yu, L.; Cai, Y.; Wang, H.; Pan, L.; Li, J.; Chen, S.; Liu, Z.; Han, F.; Li, B. Biomimetic Bone Regeneration Using Angle-Ply Collagen Membrane-Supported Cell Sheets Subjected to Mechanical Conditioning. *Acta Biomater.* **2020**, *112*, 75–86. https://doi.org/10.1016/j.actbio.2020.05.041.
(35) Klein-Nulend, J.; Bacabac, R.; Bakker, A. Mechanical Loading and How It Affects Bone Cells: The Role of the Osteocyte Cytoskeleton in Maintaining Our Skeleton. *Eur. Cell. Mater.* **2012**, *24*, 278–291. https://doi.org/10.22203/eCM.v024a20.
(36) Shapiro, F.; Wu, J. Y. Woven Bone Overview: Structural Classification Based on Its Integral Role in Developmental, Repair and Pathological Bone Formation throughout Vertebrate Groups. *Eur Cell Mater* **2019**, *38*, 137–167. https://doi.org/10.22203/eCM.v038a11.
(37) Schädli, G. N.; Vetsch, J. R.; Baumann, R. P.; de Leeuw, A. M.; Wehrle, E.; Rubert, M.; Müller, R. Time-Lapsed Imaging of Nanocomposite Scaffolds Reveals Increased Bone Formation in Dynamic Compression Bioreactors. *Commun. Biol.* **2021**, *4* (1), 110. https://doi.org/10.1038/s42003-020-01635-4.
(38) Song, I.-W.; Nagamani, S. C. S.; Nguyen, D.; Grafe, I.; Sutton, V. R.; Gannon, F. H.; Munivez, E.; Jiang, M.-M.; Tran, A.; Wallace, M.; Esposito, P.; Musaad, S.; Strudthoff, E.; McGuire, S.; Thornton, M.; Shenava, V.; Rosenfeld, S.; Huang, S.; Shypailo, R.; Orwoll, E.; Lee, B. Targeting TGF-**β** for Treatment of Osteogenesis Imperfecta. *J. Clin. Invest.* **2022**, *132* (7). https://doi.org/10.1172/JCI152571.
(39) Zhytnik, L.; Maasalu, K.; Reimann, E.; Märtson, A.; Kõks, S. RNA Sequencing Analysis Reveals Increased Expression of Interferon Signaling Genes and Dysregulation of Bone Metabolism Affecting Pathways in the Whole Blood of Patients with Osteogenesis Imperfecta. *BMC Med. Genomics* **2020**, *13* (1), 177. https://doi.org/10.1186/s12920-020-00825-7.
(40) Kumar, P.; Satyam, A.; Fan, X.; Collin, E.; Rochev, Y.; Rodriguez, B. J.; Gorelov, A.; Dillon, S.; Joshi, L.; Raghunath, M.; Pandit, A.; Zeugolis, D. I. Macromolecularly Crowded in Vitro Microenvironments Accelerate the Production of Extracellular Matrix-Rich Supramolecular Assemblies. *Sci. Rep.* **2015**, *5* (1), 8729. https://doi.org/10.1038/srep08729.
(41) Bonewald, L. F. The Amazing Osteocyte. *J. Bone Miner. Res.* **2011**, *26* (2), 229–238. https://doi.org/10.1002/jbmr.320.
(42) Pennings, I.; van Dijk, L. A.; van Huuksloot, J.; Fledderus, J. O.; Schepers, K.; Braat, A. K.; Hsiao, E. C.; Barruet, E.; Morales, B. M.; Verhaar, M. C.; Rosenberg, A. J. W. P.; Gawlitta, D. Effect of Donor Variation on Osteogenesis and Vasculogenesis in Hydrogel Cocultures. *J. Tissue Eng. Regen. Med.* **2019**, *13* (3), 433–445. https://doi.org/10.1002/term.2807.
(43) Andrzejewska, A.; Catar, R.; Schoon, J.; Qazi, T. H.; Sass, F. A.; Jacobi, D.; Blankenstein,

A.; Reinke, S.; Krüger, D.; Streitz, M.; Schlickeiser, S.; Richter, S.; Souidi, N.; Beez, C.; Kamhieh-Milz, J.; Krüger, U.; Zemojtel, T.; Jürchott, K.; Strunk, D.; Reinke, P.; Duda, G.; Moll, G.; Geissler, S. Multi-Parameter Analysis of Biobanked Human Bone Marrow Stromal Cells Shows Little Influence for Donor Age and Mild Comorbidities on Phenotypic and Functional Properties. *Front. Immunol.* **2019**, *10*. https://doi.org/10.3389/fimmu.2019.02474.

(44) Gioia, R.; Panaroni, C.; Besio, R.; Palladini, G.; Merlini, G.; Giansanti, V.; Scovassi, I. A.; Villani, S.; Villa, I.; Villa, A.; Vezzoni, P.; Tenni, R.; Rossi, A.; Marini, J. C.; Forlino, A. Impaired Osteoblastogenesis in a Murine Model of Dominant Osteogenesis Imperfecta: A New Target for Osteogenesis Imperfecta Pharmacological Therapy. *Stem Cells* **2012**, *30* (7), 1465–1476. https://doi.org/10.1002/stem.1107.

(45) Callens, S. J. P.; Fan, D.; van Hengel, I. A. J.; Minneboo, M.; Diaz-Payno, P. J.; Stevens, M. M.; Fratila-Apachitei, L. E.; Zadpoor, A. A. Emergent Collective Organization of Bone Cells in Complex Curvature Fields. *Nat Commun* **2023**, *14* (1), 855. https://doi.org/10.1038/s41467-023-36436-w.

(46) Rougerie, P.; Silva dos Santos, R.; Farina, M.; Anselme, K. Molecular Mechanisms of Topography Sensing by Osteoblasts: An Update. *Appl. Sci.* **2021**, *11* (4), 1791. https://doi.org/10.3390/app11041791.

(47) Jensen, C.; Teng, Y. Is It Time to Start Transitioning From 2D to 3D Cell Culture? *Front. Mol. Biosci.* **2020**, *7*. https://doi.org/10.3389/fmolb.2020.00033.

(48) Fratzl-Zelman, N.; Misof, B. M.; Klaushofer, K.; Roschger, P. Bone Mass and Mineralization in Osteogenesis Imperfecta. *Wien Med Wochenschr* **2015**, *165* (13–14), 271–277. https://doi.org/10.1007/s10354-015-0369-2.

(49) Blouin, S.; Fratzl-Zelman, N.; Glorieux, F. H.; Roschger, P.; Klaushofer, K.; Marini, J. C.; Rauch, F. Hypermineralization and High Osteocyte Lacunar Density in Osteogenesis Imperfecta Type V Bone Indicate Exuberant Primary Bone Formation. *J Bone Min. Res* **2017**, *32* (9), 1884–1892. https://doi.org/10.1002/jbmr.3180.

(50) Jiang, H.; Zhang, Z.; Yu, Y.; Chu, H. Y.; Yu, S.; Yao, S.; Zhang, G.; Zhang, B. T. Drug Discovery of DKK1 Inhibitors. *Front Pharmacol* **2022**, *13*, 847387. https://doi.org/10.3389/fphar.2022.847387.

(51) van Lenthe, H.; Hagenmüller, H.; Bohner, M.; Hollister, S. J.; Meinel, L.; Müller, R. Nondestructive Micro-Computed Tomography for Biological Imaging and Quantification of Scaffold–Bone Interaction in Vivo. *Biomaterials* **2007**, *28* (15), 2479–2490. https://doi.org/10.1016/j.biomaterials.2007.01.017.

(52) Liu, Q.; Li, M.; Wang, S.; Xiao, Z.; Xiong, Y.; Wang, G. Recent Advances of Osterix Transcription Factor in Osteoblast Differentiation and Bone Formation. *Front. Cell Dev. Biol.* **2020**, *8*. https://doi.org/10.3389/fcell.2020.601224.

(53) Zhang, C.; Dai, H.; de Crombrugghe, B. Characterization of Dkk1 Gene Regulation by the Osteoblast-Specific Transcription Factor Osx. *Biochem. Biophys. Res. Commun.* **2012**, *420* (4), 782–786. https://doi.org/10.1016/j.bbrc.2012.03.073.

(54) Shapiro, F.; Maguire, K.; Swami, S.; Zhu, H.; Flynn, E.; Wang, J.; Wu, J. Y. Histopathology of Osteogenesis Imperfecta Bone. Supramolecular Assessment of Cells and Matrices in the Context of Woven and Lamellar Bone Formation Using Light, Polarization and Ultrastructural Microscopy. *Bone Rep.* **2021**, *14*, 100734. https://doi.org/10.1016/j.bonr.2020.100734.

(55) Semler, O.; Hoyer-Kuhn, H.; Doetsch, J.; Schoenau, E. Personalized Medicine in Patients with Osteogenesis Imperfecta. *Mol. Cell. Pediatr.* **2014**, *1* (1), A10. https://doi.org/10.1186/2194-7791-1-S1-A10.

(56) Lim, P. J.; Marfurt, S.; Lindert, U.; Opitz, L.; Ndarugendamwo, T.; Srikanthan, P.; Poms, M.; Hersberger, M.; Langhans, C.-D.; Haas, D.; Rohrbach, M.; Giunta, C. Omics Profiling of S2P Mutant Fibroblasts as a Mean to Unravel the Pathomechanism and Molecular

Signatures of X-Linked MBTPS2 Osteogenesis Imperfecta. *Front. Genet.* **2021**, *12*. https://doi.org/10.3389/fgene.2021.662751.
(57) Dalby, M. J.; Gadegaard, N.; Oreffo, R. O. C. Harnessing Nanotopography and Integrin–Matrix Interactions to Influence Stem Cell Fate. *Nat. Mater.* **2014**, *13* (6), 558–569. https://doi.org/10.1038/nmat3980.
(58) Besio, R.; Garibaldi, N.; Leoni, L.; Cipolla, L.; Sabbioneda, S.; Biggiogera, M.; Mottes, M.; Aglan, M.; Otaify, G. A.; Temtamy, S. A.; Rossi, A.; Forlino, A. Cellular Stress Due to Impairment of Collagen Prolyl Hydroxylation Complex Is Rescued by the Chaperone 4-Phenylbutyrate. *Dis. Model. Mech.* **2019**, *12* (6), dmm038521. https://doi.org/10.1242/dmm.038521.
(59) Garibaldi, N.; Besio, R.; Pirota, V.; Albini, B.; Colombo, G.; Galinetto, P.; Doria, F.; Carriero, A.; Forlino, A. A Novel Chemical Chaperone Ameliorates Osteoblast Homeostasis and Extracellular Matrix in Osteogenesis Imperfecta. *Life Sci.* **2025**, *361*, 123320. https://doi.org/10.1016/j.lfs.2024.123320.
(60) Takeyari, S.; Kubota, T.; Ohata, Y.; Fujiwara, M.; Kitaoka, T.; Taga, Y.; Mizuno, K.; Ozono, K. 4-Phenylbutyric Acid Enhances the Mineralization of Osteogenesis Imperfecta iPSC-Derived Osteoblasts. *J Biol Chem* **2021**, *296*, 100027. https://doi.org/10.1074/jbc.RA120.014709.
(61) Takahashi, T. Organoids for Drug Discovery and Personalized Medicine. *Annu Rev Pharmacol Toxicol* **2019**, *59*, 447–462. https://doi.org/10.1146/annurev-pharmtox-010818-021108.
(62) T. Sato H. Clevers. Growing Self-Organizing Mini-Guts from a Single Intestinal Stem Cell: Mechanism and Applications. *Science* **2013**, *340*. https://doi.org/10.1126/science.1234852.
(63) Dekkers, J. F.; Wiegerinck, C. L.; de Jonge, H. R.; Bronsveld, I.; Janssens, H. M.; de Winter-de Groot, K. M.; Brandsma, A. M.; de Jong, N. W. M.; Bijvelds, M. J. C.; Scholte, B. J.; Nieuwenhuis, E. E. S.; van den Brink, S.; Clevers, H.; van der Ent, C. K.; Middendorp, S.; Beekman, J. M. A Functional CFTR Assay Using Primary Cystic Fibrosis Intestinal Organoids. *Nat. Med.* **2013**, *19* (7), 939–945. https://doi.org/10.1038/nm.3201.
(64) Berkers, G.; van Mourik, P.; Vonk, A. M.; Kruisselbrink, E.; Dekkers, J. F.; de Winter-de Groot, K. M.; Arets, H. G. M.; Marck-van der Wilt, R. E. P.; Dijkema, J. S.; Vanderschuren, M. M.; Houwen, R. H. J.; Heijerman, H. G. M.; van de Graaf, E. A.; Elias, S. G.; Majoor, C. J.; Koppelman, G. H.; Roukema, J.; Bakker, M.; Janssens, H. M.; van der Meer, R.; Vries, R. G. J.; Clevers, H. C.; de Jonge, H. R.; Beekman, J. M.; van der Ent, C. K. Rectal Organoids Enable Personalized Treatment of Cystic Fibrosis. *Cell Rep* **2019**, *26* (7), 1701-1708 e3. https://doi.org/10.1016/j.celrep.2019.01.068.
(65) Dyment, N. A.; Jiang, X.; Chen, L.; Hong, S. H.; Adams, D. J.; Ackert-Bicknell, C.; Shin, D. G.; Rowe, D. W. High-Throughput, Multi-Image Cryohistology of Mineralized Tissues. *J. Vis. Exp.* **2016**, *2016* (115), 1–11. https://doi.org/10.3791/54468.
(66) Zhang, J.; Eyisoylu, H.; Qin, X.-H.; Rubert, M.; Müller, R. 3D Bioprinting of Graphene Oxide-Incorporated Cell-Laden Bone Mimicking Scaffolds for Promoting Scaffold Fidelity, Osteogenic Differentiation and Mineralization. *Acta Biomater.* **2021**, *121*, 637–652. https://doi.org/10.1016/j.actbio.2020.12.026.
(67) J. Ahrens; B. Geveci; C. Law. *ParaView An End-User Tool for Large Data Visualization*; Elsevier, 2005.
(68) Schädli, G. N.; David, H.; de Leeuw, A. M.; Carlson, F.; Tenisch, L.; Muff, P.; Rubert, M.; Müller, R. Optimizing Barium Titanate Nanocomposite Bone Scaffolds for Biomineralization in Dynamic Compression Bioreactors Using Time-Lapsed Microstructural Imaging and Smart Thresholding. *Front. Mater.* **2022**, *8* (February), 1–15. https://doi.org/10.3389/fmats.2021.796044.
(69) Liao, Y.; Smyth, G. K.; Shi, W. The Subread Aligner: Fast, Accurate and Scalable Read

Mapping by Seed-and-Vote. *Nucleic Acids Res* **2013**, *41* (10), e108. https://doi.org/10.1093/nar/gkt214.
(70) Liao, Y.; Smyth, G. K.; Shi, W. featureCounts: An Efficient General Purpose Program for Assigning Sequence Reads to Genomic Features. *Bioinformatics* **2014**, *30* (7), 923–930. https://doi.org/10.1093/bioinformatics/btt656.
(71) Love, M. I.; Huber, W.; Anders, S. Moderated Estimation of Fold Change and Dispersion for RNA-Seq Data with DESeq2. *Genome Biol* **2014**, *15* (12), 550. https://doi.org/10.1186/s13059-014-0550-8.
(72) Luo, W.; Friedman, M. S.; Shedden, K.; Hankenson, K. D.; Woolf, P. J. GAGE: Generally Applicable Gene Set Enrichment for Pathway Analysis. *BMC Bioinformatics* **2009**, *10*, 161. https://doi.org/10.1186/1471-2105-10-161.
(73) Kamburov, A.; Pentchev, K.; Galicka, H.; Wierling, C.; Lehrach, H.; Herwig, R. ConsensusPathDB: Toward a More Complete Picture of Cell Biology. *Nucleic Acids Res* **2011**, *39* (Database issue), D712-7. https://doi.org/10.1093/nar/gkq1156.